EXPERIMENTAL AND THEORETICAL STUDY OF NUCLEAR REACTION RATES IN THE RP-PROCESS

By

Alan Matthew Amthor

A DISSERTATION

Submitted to
Michigan State University
in partial fulfillment of the requirements
for the degree of

DOCTOR OF PHILOSOPHY

Department of Physics and Astronomy

2008

ABSTRACT

EXPERIMENTAL AND THEORETICAL STUDY OF NUCLEAR REACTION RATES IN THE RP-PROCESS

By

Alan Matthew Amthor

Proton rich nuclei ^{37}Ca and ^{36}K have been studied by single neutron removal from a radioactive cocktail beam produced at the National Superconducting Cyclotron Laboratory. The excited state structure of each nucleus near the proton threshold was determined by in-flight gamma spectroscopy. The uncertainty in the ^{35}Ar(p,γ)^{36}K and ^{36}K(p,γ)^{37}Ca reaction rates, important at early times in the *rp*-process in Type-I X-ray bursts, have been reduced dramatically, and the ^{36}K(p,γ)^{37}Ca rate has increased by up to 4 orders of magnitude for burst temperatures. Under burst conditions these reaction rates are dominated by resonant capture contributions from individual resonances because of the low level density just above the proton threshold in the proton-rich compound nucleus. Therefore, precise structure measurements are required to reduce the orders of magnitude rate uncertainty in these key reactions and thereby constrain X-ray burst models. The resulting level scheme for ^{37}Ca includes six previously unmeasured states and the implications for burst observations and A = 37, T = 3/2 isobaric mass quartets are discussed. The first excited state in ^{36}Ca was coincidentally observed, with improved precision at 3045.0 (2.4) keV.

A comprehensive study of the dependence of simulated Type I X-ray bursts lightcurves on individual uncertain (p,γ) and (α,p) reaction rates along the *rp*-process path has been performed. A two-step process was employed using a specially calibrated version of the single-zone burst model of Schatz et al. [1] to identify sensitive rates from the full set of rates involved. These were followed by multi-zone simulations in the KEPLER burst code of entire sequences of bursts to consider observable

changes both at the onset of bursting behavior and under steady state bursting conditions. Several rate sensitivities were identified in the single accretion model of solar metallicity material accreted at a rate of 1.75 $\times 10^{-9} M_{\odot}$ per year, and the rate sensitivity of the calibrated single-zone burst model shows great similarity to that of the multi-zone model.

For Christ and His kingdom.

"He is the image of the invisible God, the firstborn over all creation.
For by him all things were created:
things in heaven and on earth, visible and invisible...
He is before all things, and in him all things hold together."

—Paul the apostle's letter to the Church at Colossae

ACKNOWLEDGMENTS

Contents

List of Figures

Images in this dissertation are presented in color.

List of Tables

Chapter 1

Introduction

1.1 Motivation

The universe is awash in nuclear matter, protons and neutrons bound in a delicate interplay of electromagnetic and nuclear forces. The nucleus is a structure simple in its conception, protons and neutrons interacting through a strong force, but of daunting true complexity. The nucleus is a quantum many-body problem which evades exact solution and is solved numerically by ab initio methods for only the lightest isotopes. This is notwithstanding the careful study of the properties of over (1300) test cases in the stable and unstable isotopes throughout the approximately 50-year history of the field of nuclear science. Although we now know that baryonic matter, the category that includes atoms, comprises a comparably small fraction of the total matter in the universe, it is this baryonic matter that is most easily directly observed and most directly affects humanity. This is the stuff of the periodic table and the material of which we ourselves are composed.

In answering these questions, we quickly find that our understanding of the universe is closely connected to our understanding of atomic nuclei. The apparent fact that the Big Bang produced mostly hydrogen, helium and a small amount of lithium is well modeled by reactions involving the lightest elements [2]. The lifetimes and

energy output of stars can be well modeled by a series of nuclear burning processes, first involving hydrogen, then helium, etc. up through iron [3]. However, much of the universe is not understood quantitatively. In particular we lack accurate models of explosive events such as supernovae (of all types), novae, and X- and gamma-ray bursts. The explosive burning (the series of nuclear reactions) that takes place in these environments is a challenge to model both because of the computational complexity and because we lack a basic understanding of many of the nuclei involved.

The persisting uncertainties in nuclear structure that hamper our efforts to understand the workings of the universe could be answered by a comprehensive effort at nuclear structure modelling. Theoretical models are used to predict nuclear masses, half-lives, excitation structures and so on. Though these models are all based on experimental data in one way or another, the further one goes from the valley of β stability (where isotopes are energetically stable and do not decay by the weak interaction) beyond experimental information, the longer the arm of the extrapolation and consequently the larger the uncertainties in the predicted values. Our ability to experimentally study ever more nuclear species, pushing towards and beyond the bounds of particle stability, the drip lines (where additional neutrons or protons are not bound in a nucleus and are spontaneously emitted), in an effort to constrain theoretical models, is continually expanding, but large gains come only at a punctuated pace as new facilities become available or new techniques are pioneered.

Nuclear properties at or near the drip-lines are a necessary input to computational models of explosive burning scenarios. These uncertainties leave models of such astrophysical processes more weakly constrained than current observations. For example, several type I x-ray burst sources have been observed over long chains of bursts to produce confidence intervals of the burst lightcurve with errors of better than 2.5% [4], while lightcurves from burst models can shift by this amount or more based on the current uncertainty of only a single proton capture reaction rate (see e.g. Chapter 5). Thus to take full advantage of progress in observations and modelling

of astrophysical events, we must make an effort to reduce the uncertainties in the nuclear physics inputs.

1.2 Astrophysics

Just as astrophysics turns to nuclear physics in its quest to understand the heavens, so too has nuclear physics turned to events of the greatest scale to test and improve its understanding of the femto scale. All the elements of the universe, from the lightest to the heaviest, found their birth in astrophysical realms, from the earliest moments of big bang nucleosynthesis, whose ripples are seen in the cosmic microwave background, to the cores of the great gravitational cauldrons of Population I stars and the luminous supernovae—thought to be the site of the rapid neutron capture process responsible for producing most of the heavy elements beyond iron—that we can observe today. Not surprisingly, the better part of galactic chemical evolution takes place under the most extreme physical conditions present in the universe. Consequently, these astrophysical events offer a view of processes involving asymmetric nuclear matter that we are decades or centuries away from successfully studying in the laboratory. Observation of these systems together with well constrained multi-physics models may yield insight on the nature of the nuclear force, just as the combination of a well constrained solar model and careful observation led to the discovery of neutrino oscillations.

Type I X-ray bursts are one such dramatic astrophysical event and are both the motivation and partly the subject of this work. These explosive events occur in the shallow surface layers (specifically referred to as the outer atmosphere [5]) of neutron stars in binary systems where the neutron star accretes matter from it's main sequence companion. The neutron star itself is an object of immense interest to nuclear physics. It represents a unique example of macroscopic nuclear matter—with internal densities comparable to that of the atomic nucleus—driven to an extreme of isospin by electron

capture in the crust [6]. The exact nature of the interior is unknown, as is the precise relation of the mass and radius (and consequently the surface gravity). More precise determination of the neutron star structure would improve our understanding of the nuclear matter equation of state.

Type I X-ray bursts, while fairly superficial, are affected by the surface gravity, due to the effects of general relativity. Burst fluence oscillations on the millisecond timescale from bursts on rapidly rotating neutron stars and photospheric radius expansion bursts, where the radiation pressure overcomes the surface gravity are two other examples of connections between burst observations and neutron star structure. The current state of X-ray burst models is unfortunately not yet adequate to use these observations to infer the neutron star's properties. Work has just begun on non-spherical models of neutron stars, that hope to use information from surface oscillations to infer the neutron star's properties, but to date all burst codes are spherically symmetric.

Nearly all of the nuclear burning that drives these bursts takes place at extreme conditions of temperature and density in regions of proton or helium excess, such that the flow of nuclear material goes largely through extreme forms of nuclear matter not observed on earth and difficult to access in experiments. The properties of these radioactive isotopes that determine the properties of Type I X-ray bursts—the burning that takes place there, the isotopic abundances and energy produced, as well as the observed luminosity—are largely unknown to nuclear science. This unknown nuclear physics input also leaves the models insufficiently constrained to take full advantage of ever improving burst observations to infer the neutron star structure.

In the experimental portion of this work we study one nuclear physics input, the ^{36}K(p,γ)^{37}Ca reaction rate. The uncertainty is reduced by orders of magnitude by measuring the excited state structure above the proton threshold. As will be discussed further later, the proton capture reaction rates dominated by resonant capture depend exponentially on the energies of these states, easily yielding rate uncertainties of four

orders of magnitude based on shell model calculated level uncertainties on the order of 150 keV.

Experimental resources are limited however, so in a later chapter we study which of the thousands of individual (p,γ) and (α,p) reaction rate uncertainties are most critical in our efforts to constrain burst models. These two types of rates are not the only important nuclear physics uncertainties in burst models. Work is also needed on the triple-α reaction rate, which provides the seed nuclei for the rp- and αp-processes that power X-ray bursts, as well as β-decay half-lives, inverse reaction rates, etc.; though these are not the focus of this work.

Progress in reducing the nuclear physics uncertainties can enable just the type of precision in modelling of Type I X-ray bursts and related crust processes that is necessary to probe the physical properties of this macroscopic nuclear system, by calibrating burst models and cooling models to observations. Large amounts of diverse observational data are available, and the first steps in three dimensional modelling of the burst layer have been taken. Still, nuclear physics experiments will be the final key in opening the door to an era of precision neutron star modelling.

Chapter 2

The *rp*-Process in Type I X-Ray Bursts

2.1 Introduction

Type I X-ray Bursts are the most frequent thermonuclear explosions in the Universe. They are generally periodic, short-duration x-ray pulses, lasting from 10–200 seconds, with luminosities of the order of the Eddington luminosity ($F_{Edd} = 1.8{\times}10^{38}$ erg/s for a typical neutron star with $M = 1.4M_{\odot}$) and recurrence times typically from hours to days [7–9]. The source of these pulses is unstable burning in the shallow surface layers of accreting neutron stars [10, 11]. As the accreted material is steadily burned and continually subsumed in the neutron star ocean, for a certain range of mass transfer rates [12], an unstable burning condition is reached at the base of the column of accreted fuel [10]. This unstable burning then rapidly processes a large fraction of the accreted nuclear material through the *rp*-process and/or the αp-process.

The nuclear burning in these rapid fusion processes involves a wide range of nuclear species from stable isotopes to the proton drip-line. The process is sensitive to uncertain structure and reaction properties near and beyond the current frontier of experimental knowledge. Identifying and reducing these uncertainties is key to

constraining models of nuclear structure and mass and thereby burst models so that these may then be used as a framework to interpret the global bursting behavior, including an absolute calibration of the burst luminosity, and subsequently to constrain models of the deeper neutron star crust processes as well as the bulk properties of the neutron star itself. The neutron star surface lies at an interface with macroscopic nuclear matter and may be able to shed light on the nuclear matter equation of state. Calibrating models to observations absolutely could allow the use of Type I bursts as standard candles [13] or eventually provide information on the central density by way of the redshift which is determined by the surface gravity. Some of the physical parameters of the binary systems might be derivable from well constrained models, providing a possible connection to theories of galactic evolution through the number and nature of binaries.

It was only a few years after the initial discovery of X-ray bursts, and the first structural understanding of their source, that the *rp*-process was suggested as the source of energy in these events [11]. Since then, considerable effort has gone to developing an understanding of bursting systems' behavior as a function of their inferred astrophysical properties (neutron star mass and radius, accretion rate $\dot{M}$, accreted composition, and the thermal structure of the crust). The current status of this work will be discussed further in the following sections.

Work toward a consistent theoretical understanding of X-ray bursts is carried out largely through the development of computer models; though some properties can still be explored analytically (see e.g. [14]). The physical system being studied involves a large expanse of phase space, isotopes from a large fraction of the full nuclear landscape, with highly variable abundances each strongly coupled to the current and past thermodynamic properties of the neutron star ocean, thermodynamic properties which themselves often vary on extremely short time and length scales. Because of this, current computational resources require some significant reduction of this full space by way of some simplifying assumptions. Thus all current simulations are

limited in some way, making it impossible to consider all of the system properties simultaneously. For example, all nuclear burning burst model calculations to date have assumed spherical symmetry, even though observed ms-oscillations of burst fluence argue for spherical asymmetry.Work has just recently begun on higher dimensional effects on the neutron star surface, e.g. compressional surface modes. The remaining one spacial dimension is also neglected in the case of single-zone models, which include no radial variation of system properties. While these can be run much more quickly, they cannot properly treat radiation transport to the surface or include the effects of compositional inertia. Constant temperature models are sometimes used and can offer reasonable approximations of nuclear reaction flows in steady state rp-process burning or at certain times during the burst rp-process [15].

The multi-zone KEPLER model [16] includes a full nuclear reaction network coupled to a multi-zone hydrodynamics code and is thus quite computation-intensive, requiring several CPU hours to simulate a single burst, while simpler models may be run in a matter of CPU seconds. This restricts the number of parameter variations that may be considered and suggests the use of simpler models for broader studies of accretion models or input uncertainties.

The ultimate goal of burst models is to reliably reproduce astrophysical observations of sites that may be considered macroscopic nuclear physics laboratories. Precision x-ray observatories have to date recorded a great variety of type I bursting behavior, which is just now starting to be compared directly to the results of multi-zone burst models [17]. The success of continuing efforts to constrain the astrophysical properties of these sources and their utility in gaining insight into related questions in nuclear physics, astrophysics, and cosmology depends on constraining the most critical uncertainties in the nuclear physics inputs.

Many of the nuclear reaction rates and nuclear structure properties used in X-ray burst models have not been experimentally determined but are rather estimated within various theoretical frameworks. These uncertainties limit our ability to con-

strain model dependent deficiencies. β-decay lifetimes and (p,γ) and (α,p) reaction rates for individual nuclides along the reaction pathway can strongly influence the energy generation, dominant reaction pathway, and final nucleosynthesis of the entire process. Because of broad and continuing progress in experimental methods with radioactive ion beams, many previously estimated quantities of interest can now be measured directly.

Considering reaction rates in particular, the large number of uncertain rates along the *rp*- and αp-process paths require that experimental studies focus on those most critical in the burst process (i.e., those whose variation within their uncertainty leads to the greatest change in observable burst properties). In this work, the single-zone model of Schatz et al. [15] was used with 1697 individual proton capture rate variations to identify those with the greatest impact on the burst lightcurve. These were then considered in the multi-zone KEPLER X-ray burst model. This sensitivity study is discussed further in Chapter 5. The experimental study to be discussed in Chapter 3 was motivated by previous burst model studies.

2.2 Theory

The progress of a standard Type I X-ray burst event may be summarized in a few steps. During the stable burning phase prior to burst ignition, material is continuously building on the surface of the neutron star according to the total mass accretion rate, $\dot{\mathrm{M}}$. The non-burst luminosity is determined almost entirely by $\dot{\mathrm{M}}$ and the surface gravity of the neutron star, even though nuclear reactions are certainly generating energy during this phase, since the amount of gravitational energy released is much larger ($GM_{\mathrm{NS}}m_p/r_{\mathrm{NS}} \approx 200$ MeV/nucleon) than the maximum of nuclear binding. The amount that nuclear reactions will actually contribute to the off-burst fluence depends largely on the metallicity—more specifically the isotopic abundances—of the accreted material, the energy lost to neutrinos, and the endpoint of the reaction

network. For a solar abundance distribution burned to heavy elements, the total energy released by nuclear reactions is about 5 MeV/nucleon.

The accretion metallicity and the temperature at the base of the accreted fuel column will determine the dominant method of stable nuclear burning, whether by the triple-α reaction or through the standard or β-limited CNO cycle. As the depth of the hydrogen or helium burning column increases (measured in g/cm^2 from the neutron star surface) the temperature and density at the base continually increases. The thin burning shells cannot cool by either expansion or by electrons due to their degeneracy. This creates a situation wherein the temperature sensitivity of the rate of cooling becomes substantially less than the temperature sensitivity of the exoergic nuclear reaction processes [18]. This is the "thin-shell" burning instability [10] that precipitates thermonuclear runaway in the neutron star atmosphere [5]. The energy not removed from the burning zone will increase the local temperature, thus further increasing the rate of energy generation beyond the local cooling in a feedback loop until the system has time to cool by expansion or fuel is exhausted. This is the process that ignites the burst. For a short time the luminosity of the neutron star will increase dramatically as large fractions of the previously accumulated light elements are converted to heavier elements through rapid unstable H and/or He burning.

Given the variability in x-ray bursts from system to system, it is important to consider what system parameters determine the observed characteristics and through what processes. Qualities to consider include the total accretion rate in the binary system ($\dot{\mathrm{M}}$), the specific accretion rate ($\dot{m} = \dot{M}/Area_{acc}$), the ratio of total persistent flux to total burst flux from the neutron star surface ($\alpha = E_p/E_b$), the neutron star mass and radius, the light curve, the burst duration, the recurrence time, and the burst regularity.

2.2.1 Burst Scenarios

There is some variety in x-ray bursts depending on the astrophysical parameters of the system. The total mass accretion rate, $\dot{\mathrm{M}}$ is related to the persistent luminosity (measured far from a burst event) through the gravitational energy release, $GM\dot{\mathrm{M}}/R$. For an archetypal neutron star with $M \approx 1.4M_{\odot}$ and $R \approx 10km$, the energy release per accreted nucleon is $GMm_p/R \approx 200MeV$. $\dot{\mathrm{M}}$, together with the composition of the accreted material, also sets the amount of nuclear energy available through exoergic reaction processes. α is defined as the ratio of the persistent flux to burst flux. In an approximation assuming constant gravitational energy release during a burst and neglecting the nuclear energy release far from the burst event, the quantity α gives the proportion of gravitational energy release to nuclear energy release. The value of α inferred from observations is consistent with the approximate ratio of accretion to nuclear energy generation expected from the above basic considerations.

For shorter recurrence times and higher accretion rates, the bulk of nuclear burning takes place during the bursts and α is a measure of the metallicity of the accreted material. In the case with $\alpha \approx 40$ the accreted material must be predominantly hydrogen (e.g. a solar composition), while much larger mass fractions of He in accreted matter will lead to larger values of α (for pure He, $\alpha \approx 120$), since the material already has binding energy which is a significant fraction of the maximum nuclear binding energy per nucleon. Observations of systems with higher α values are consistent with more He dominated bursts, which are generally of shorter duration (10–40 seconds). For systems where significant fractions of the nuclear fuel are burned outside of burst events, as is the case for longer recurrence times and lower accretion rates, higher α values will result for any given accretion metallicity.

The global accretion rate determines the off-burst temperature and density evolution in the burning shell of the neutron star, by setting the rate of increase of column depth. In the same way $\dot{\mathrm{M}}$ also determines the amount of time necessary for a critical density and temperature condition to be reached near the column's base, which pre-

cipitates the burst. This relationship is not as simple as might be assumed. In fact, the method of ignition and the very presence of bursts depend on $\dot{\mathrm{M}}$ [12, 18]. It may be helpful to delineate a few broad categories of bursts by their ignition condition. For a given metallicity of accreted material, the bursts will be characterized by the global accretion rate. For $Z_{CNO} \approx 0.01$ the three regimes, based on simple analytical models, are as follows [8].

- For $\dot{M} \lesssim 2 \times 10^{-10} M_{\odot}\,\mathrm{yr}^{-1}$, the temperature $T < 8 \times 10^{7}$ K in the accreted layer is such that the CNO cycle hydrogen burning rate is still temperature sensitive, and the burst ignition will be by unstable hydrogen burning.

- For $\dot{M} \gtrsim 2 \times 10^{-10} M_{\odot}\,\mathrm{yr}^{-1}$, the temperature $T > 8 \times 10^{7}$ K in the accreted layer is high enough that hydrogen burning is proceeding by the β-limited CNO cycle. That is to say that at this temperature the burning rate becomes insensitive to temperature, because the β-decays in the cycle, $^{14}\mathrm{O}(\beta^{+}\nu)^{14}\mathrm{N}$ and $^{15}\mathrm{O}(\beta^{+}\nu)^{15}\mathrm{N}$, proceed much slower than the proton capture reactions. In this case the burst will be initiated by unstable He burning, which involves no weak interactions and has high temperature sensitivity. The nature of the burst in this range of $\dot{\mathrm{M}}$ depends on whether the recurrence time is greater or less than the lifetime of hydrogen in the ignition layer. The reaction chain of the burst begins with breakout from the CNO cycle through α-capture reactions, either $^{14}\mathrm{O}(\alpha,\mathrm{p})^{17}\mathrm{F}$ or $^{15}\mathrm{O}(\alpha,\gamma)^{19}\mathrm{Ne}$. If the recurrence time, t_{rec}, is longer than the time required to burn the hydrogen through the stable β-limited CNO cycle, τ_H, then the burst will involve pure He shell ignition. This would typically occur for accretion rates $2 \times 10^{-10} M_{\odot}\,\mathrm{yr}^{-1} \lesssim \dot{M} \lesssim 4.4 \times 10^{-10} M_{\odot}\,\mathrm{yr}^{-1}$.

- For $\dot{M} \gtrsim 4.4 \times 10^{-10} M_{\odot}\,\mathrm{yr}^{-1}$, generally $t_{rec} < \tau_H$ and the He triggered burst will result in runaway hydrogen and helium burning reactions through the *rp*-process.

The final category of mixed H and He bursts are the type considered in the model

calculations in the sensitivity study that is discussed in Chapter 5. For much higher accretion rates near the Eddington mass accretion rate ($\dot{M}_{Edd} \approx 2 \times 10^{-8} M_{\odot}\,\mathrm{yr}^{-1}$), stable hydrogen and helium burning will replace bursting behavior altogether [7].

Here it is important to note a distinction between $\dot{\mathrm{M}}$, which determines the persistent luminosity, and $\dot{\mathrm{m}}$=$\dot{\mathrm{M}}/\mathrm{A}_{\mathrm{acc}}$ which determines the burning conditions in a given column of accreted fuel. This distinction is nontrivial, since it is very likely that angular momentum conservation on the sometimes rapidly rotating neutron star or strong magnetic fields would prevent the accreted matter from assuming a radially symmetric distribution and instead cause build up at the equator or the poles. In this case, the two boundary values for $\dot{\mathrm{M}}$ to the three qualitatively different bursting regimes listed above may be converted to specific accretion rates at roughly $\dot{\mathrm{m}} = 900$ g cm^{-2} s^{-1} and $\dot{\mathrm{m}} = 2000$ g cm^{-2} s^{-1}.

2.2.2 *rp*-process Path

The *rp*-process, using the CNO isotopes produced through the 3α reaction as seed nuclei, consists of a series of proton captures and β-decays on unstable, neutron-deficient nuclei, following particularly close to the proton drip-line below mass 40. The specific path at any given point in time depends on the temperature and density in the burning zone [11, 19].

For temperatures above 5×10^8 K, the β-limited CNO cycle branches into a bi-cycle with a portion of the flow going through $^{14}\mathrm{O}(\alpha,p)^{17}\mathrm{F}(p,\gamma)^{18}\mathrm{Ne}(\beta^+\nu)\ ^{18}\mathrm{F}(p,\alpha)^{15}\mathrm{O}$. This has the dual effect of shortening the time for one cycle and increasing the proportion of Z_{CNO} contained in ^{15}O. Another change at $T \approx 0.5\times10^9$ K, which is enhanced by this increased concentration, is the start of leakage out of the cycle through the $^{15}\mathrm{O}(\alpha,\gamma)^{19}\mathrm{Ne}$ reaction. If T remains near the production threshold ($T \lesssim 0.5 \times 10^9$ K) the ^{19}Ne tends to return to the CNO cycle through sequences of (p,γ) and (p,α) reactions and β-decays. At higher temperatures and densities for which the proton

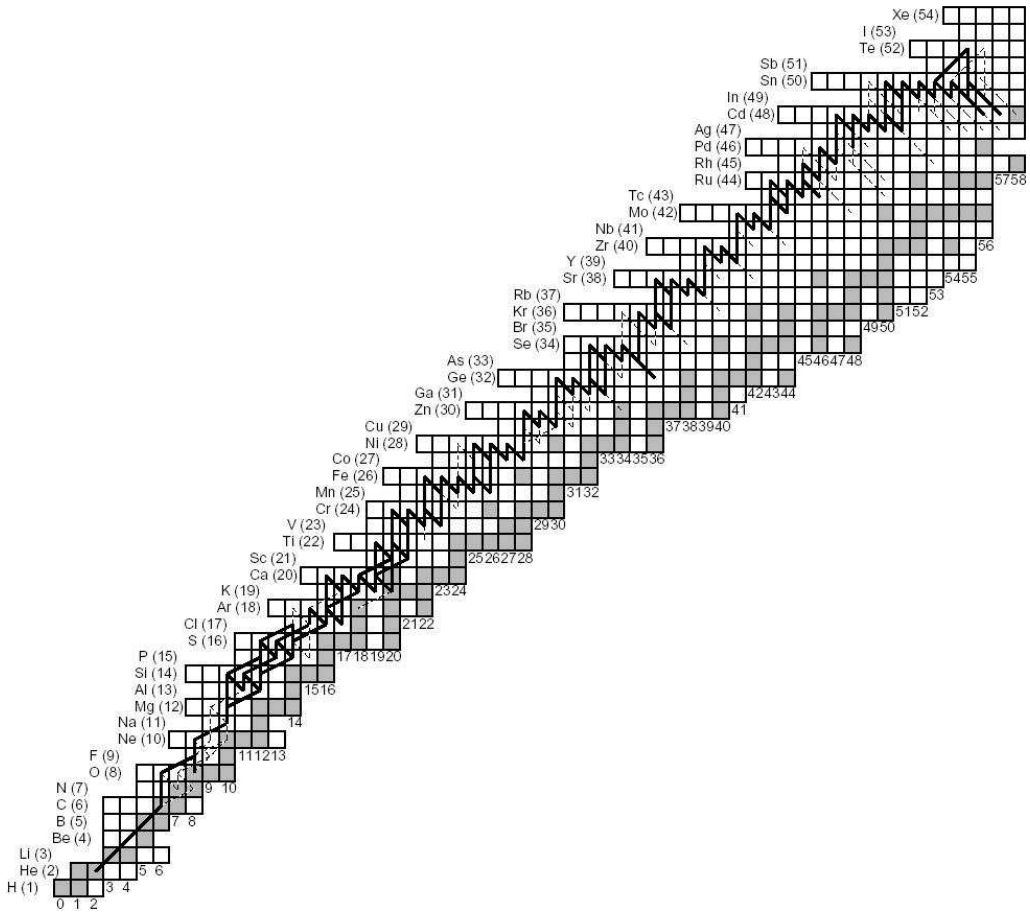

Figure 2.1: The *rp*-process begins with a fractional leakage from the CNO nuclei through α-capture. Dominant pathways of the complete *rp*-process are shown. Note the various possible bottlenecks and the bridging of certain β-decay paths by alternate (α, p) reactions. [8]

capture rate on ^{19}Ne is greater than the competing beta decay

$$\rho X_H \lambda_{(p,\gamma)}(^{19}\mathrm{Ne}) > \lambda_{e^+}(^{19}\mathrm{Ne}), \tag{2.1}$$

the ^{19}Ne is more likely to form ^{20}Na from which it will not return to the CNO cycle. As the temperature increases further, (α,p) rates become increasingly dominant over slower β^+-decay rates. This begins with the destruction of ^{18}Ne, a β^+-decay waiting point in the CNO bi-cycle, through $^{18}\mathrm{Ne}(\alpha, p)^{21}\mathrm{Na}$. For the *rp*-process this is the primary means of destruction of CNO nuclei and also the primary method of continuous feeding of the network during the burst (see Figure 2.1, since the reaction

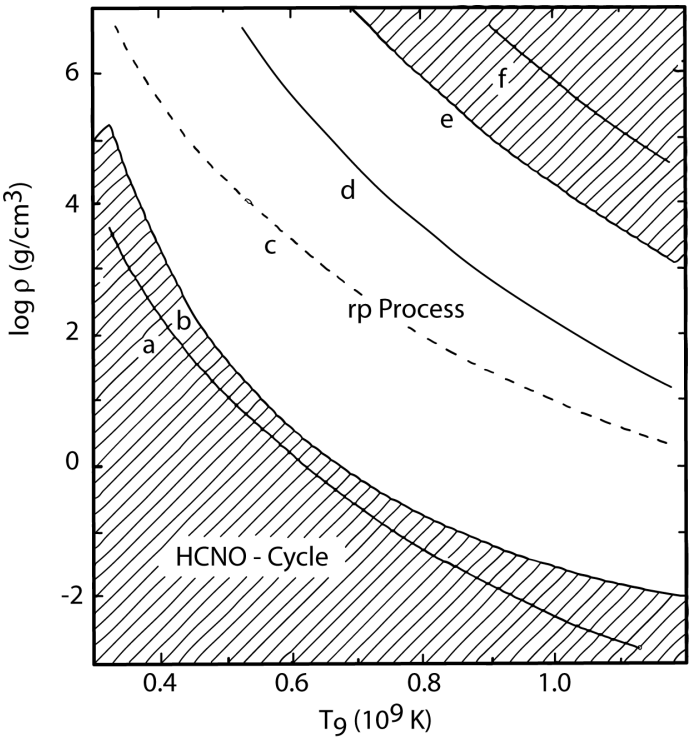

Figure 2.2: For a composition of $X_H = 0.70$ and $X_{He} = 0.28$: curve *(a)* conditions give α-capture on ^{15}O at a rate comparable to the cycling rate of the hot CNO cycle; curve *(b)* conditions give $^{19}\mathrm{Ne}(p,\gamma)$ at a rate comparable to the competing β-decay; curve *(c)* gives the point beyond which the *rp*-process rate is limited more by decay lifetimes than by the $^{15}\mathrm{O}(\alpha,\gamma)$ reaction rate; curve *(d)* conditions give four times the flow through $^{18}\mathrm{Ne}(\alpha,p)$ as through the competing β-decay; curve *(e)* conditions give over four times the rate for $^{22}\mathrm{Mg}(\alpha,p)$ as for a typical *rp*-process weak decay; and similarly curve *(f)* gives over four times the rate for $^{26}\mathrm{S}(\alpha,p)$ as for a typical *rp*-process weak decay [11].

path ending with $^{18}\mathrm{Ne}(\alpha,p)$ contains no β-decays. Initial abundances of ^{16}O, or ^{16}O previously removed from the CNO cycle, will also contribute to the *rp*-process after the burst, joining through $^{16}\mathrm{O}(p,\gamma)^{17}\mathrm{F}(p,\gamma)^{18}\mathrm{Ne}$ with ^{18}Ne continuing as before.

For $T \lesssim 0.4$ GK and $\rho \approx 1 \times 10^6\, g/cm^3$ (the typical density for *rp*-process burning in Type I bursts) the rate of the *rp*-process is still limited by the α-capture rates on oxygen that leak material from the hot CNO cycle. Beyond this point the β-decay rates become the rate limiting factor, and the *rp*-process rate becomes temporarily insensitive to increasing temperature. The 3α reaction continues to generate energy and feed material into the reaction network. As temperature continues to increase,

(α, p) reaction times decrease to match those for certain slow β^+-decays with which they compete for reaction flow, eventually becoming the dominant method of flow for an increasing span of the network through lower Z isotopes. Notable boundaries of (α, p), β^+-decay competition are shown in Figure 2.2 for ^{22}Mg(α, p) and ^{26}S(α, p), as well as ^{18}Ne(α, p), which greatly enhances leakage from the hot CNO cycle. At these points increased temperature will once again increase the reaction rate through the (α, p) reaction channels. Integrated reaction flow through lighter elements ($Z \lesssim 20$, but depending on H mass fraction) over the course of the entire burst will generally be dominated by flow through (α, p) reactions (cf. Figure 2.1).

There is appreciable reaction cycling, not only through the hot CNO cycle, but also through additional (p, α) reactions at various points competing with proton capture reactions [19]. The ever-changing, finite temperature of the environment also slows the *rp*-process through (γ, p) reactions [15]. These photodisintegration reaction rates can be determined from the proton capture reaction rates using the detailed balance principle,

$$\lambda_{i(\gamma,p)j} = (2J_p + 1)\left(\frac{\mu kT}{2\pi\hbar^2}\right)^{3/2} \exp\left(-\frac{Q_{j(p,\gamma)}}{kT}\right) \cdot \langle \sigma v \rangle_{j(p,\gamma)i}, \tag{2.2}$$

(here neglecting thermally populated excited states which will result in a scaling of the values). Note the exponential dependence on the reaction Q-value—equal to the proton separation energy of the compound nucleus in the case of capture on a target nucleus in its ground state—which decreases with increasing proximity to the proton drip line. Strong inverse photodisintegration leads to a very low equilibrium concentration of the product of a proton capture reaction, and thereby inhibits the reaction flow through that path in the network. If there are no faster alternative reaction pathways for the flow through the larger network, then the nuclide just before a strongly inhibited proton capture reaction is considered a waiting point nucleus. One example of a waiting point is ^{34}Ar, where ^{35}K has $S_p = 78$ keV. In this case

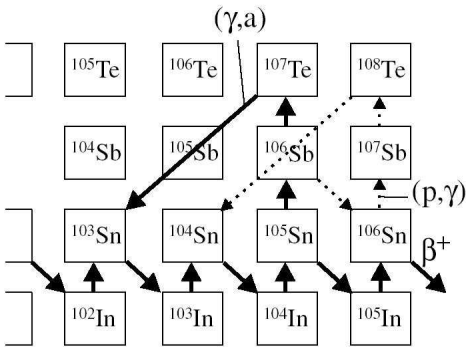

Figure 2.3: The reaction flow through the SnSbTe cycles are shown with solid lines for $> 10\%$ and dotted lines for $1 - 10\%$ of the reaction flow through the 3α reaction. [1]

$^{34}\mathrm{Ar}(\alpha, p)$ contributes substantially to the total reaction flow, notwithstanding a much higher coulomb barrier. Another key waiting point nucleus is ^{56}Ni, where ^{57}Cu has $S_p = 695keV$. Here again the reaction flow is hindered by strong photodisintegration, though at higher temperatures [19].

How far the *rp*-process nucleosynthesis will proceed in any given event will depend primarily on the supply of hydrogen in the burning zone at burst ignition. Assuming an adequate supply of hydrogen and slow cooling, the terminus of the *rp*-process in x-ray burst scenarios will be in a closed reaction cycle through Sn, Sb, and Te isotopes [1]. Shown in figures 2.1 and 2.3, the reaction flow progresses through Sn isotopes of increasing N until it reaches a point where the Sb isotope formed by proton capture is sufficiently proton-bound to resist photodisintegration, generally at ^{106}Sb but some also proceeds through ^{107}Sb. These capture a further proton to form ^{107}Te and ^{108}Te both of which decay by α-emission.

2.2.3 Relevance of Nuclear Structure

An understanding of the structure of the nuclei involved in these reactions and the systematics of the reaction processes is necessary to construct realistic models of these explosive events. In particular we require the reaction rates for capture and transfer reactions and photodisintegration as well as β-decay rates for neutron-deficient nu-

clides. Direct measurements of the reaction rates are difficult due to low production rates for most neutron deficient radioactive nuclear beams and low reaction yields. Even for the extreme temperatures present during *rp*-process burning, the peak of the Gamow-window for direct-capture is well below the energies of the Coulomb barrier.

One direct measurement of a resonant proton capture rate was performed at TRIUMF using a high intensity beam of ^{21}Na ($\approx 10^9/s$) on a hydrogen target with $E_{cm} \approx 214\,keV$. The yield, given in [20], was 5.76×10^{-12} per incident ^{21}Na, this for a resonant reaction. Larger Coulomb barriers for higher Z, lower production rates for shorter lived isotopes or refractory elements and the often considerable uncertainty of the location of the resonance to be measured all offer some explanation why direct measurements like this are not more common for *rp*-process nuclei. This measurement was of a single resonance, while even systems with low level-density will generally have 2–3 levels near the proton capture threshold that dominate the proton capture rate at some point over the range of burst temperatures (between 0.1 and 1.5 GK).

Statistical models and nuclear structure information, the latter both from experiment and from theoretical model calculations (e.g. shell model calculations), can be used to indirectly obtain reaction rates more easily for a greater variety of nuclides. Statistical model calculations are useful for capture to zones of relatively high level density. This condition is usually satisfied when the compound nucleus has a large proton separation energy, since level density increases with excitation energy. The proton separation energy naturally decreases with increasing proximity to the driplines. One such statistical model which is widely used is that of Hauser-Feshbach. For lower level densities (see Figure 2.4), statistical approaches remain valid only for very high temperatures, while at lower temperatures the direct-capture contribution and the effect of individual energy levels become significant. In these cases, a knowledge of the structure of individual nuclear excited states can be used to calculate the reaction rate for various burning conditions based on a combination of direct-capture rates and individual resonant capture contributions. Through these same relations,

uncertainties in nuclear structure (e.g. the excitation energy of a nuclear state) can be translated into uncertainties in the reaction rate. This will be further discussed in Section 5.2.

In all comprehensive *rp*-process considerations it will be necessary to use information from theoretical model calculations at some point due to the lack of complete experimental knowledge of the wide range of nuclear structures involved. Experimental information is particularly lacking for neutron-deficient nuclei with A > 64, where the masses and lifetimes of many *rp*-process isotopes are unknown. Large reaction rate uncertainties persist for many lower Z nuclei, especially those dominated by resonant capture when the uncertainties present in theoretically calculated resonance energies are significant [15, 21]. There is agreement on average within a factor of 2–3 between statistical model calculated cross sections and experiment for high temperatures, T $\geq 3 \times 10^9 K$, or for nuclei not in close proximity to the drip lines. Agreement remains fairly good for proton capture at lower temperatures, T $= 3 \times 10^8 K$ with N $\geq$ Z. For nuclei with N $<$ Z, low proton thresholds lead to low level densities in the Gamow window and orders of magnitude disagreement between Hauser-Feshbach and experimentally determined reaction rates. For a further discussion of statistical model calculations see [15, 22].

For low level density systems, which are particularly important at early times in the *rp*-process, unmeasured rates can be calculated based on nuclear structure information. These rates may be dominated by direct capture or resonant contributions. Direct capture rates can be calculated from extrapolated S-factors, and resonant capture rates are calculated based on the properties of the resonance states, with an exponential dependence on the resonance energy. Resonance energies are determined by the excitation energy of the resonance and the Q-value, which is the proton separation energy in the case of (p,γ) reactions. Thus the resonant capture rate depends both on the uncertainty of the excited state structure and the nuclear masses. Near the valley of β-stability, or at least close to constraints from experimental measure-

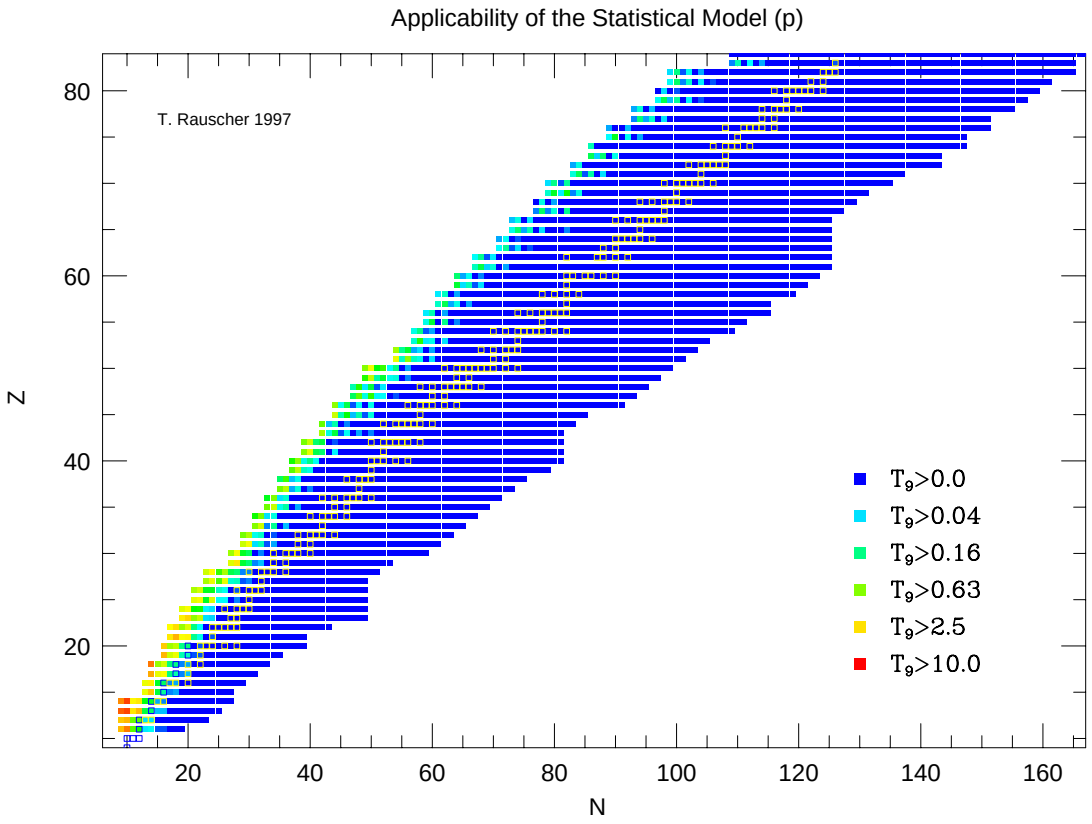

Figure 2.4: The necessary temperature is given for proton capture to provide excitation to an area of sufficient level density to make statistical model calculations valid [22]. For nuclei in the three highest temperature categories, statistical model calculations for proton capture rates should be avoided during *rp*-Process burning in type I x-ray bursts.

ments, the various mass models generally have theoretical errors of less than 100 keV. Figure 2.5 shows the source of nuclear masses used in the multi-zone code KEPLER that will be used in the sensitivity study in this work and gives a general idea of the range of uncertainties across the full rp-process path.

The excited state structure of low-Z neutron deficient nuclei which have not been experimentally determined are often calculated using a shell model code. Mirror nuclei, those isotopes across the N = Z line on the nuclear chart with the numbers of protons and neutrons reversed, can be used for a rough determination of structure information where shell model calculations are not yet available, since the excited state energies, angular momenta, and parities depend only weakly on coulomb effects

(as in [23]). Mirror states may also be used to inform and improve shell model calculations. This is particularly useful along the lower end of the *rp*-process where the mirrors are closer to stability and are frequently very well known. The effect of the coulomb force in shifting nuclear states may be calculated to infer excitation energies or mass excesses (e.g. [24]). The Isobaric Mass Multiplet Equation (see Section 4.1.2) can be used to estimate mass excesses of ground or excited states based on the isobaric analog states in neighboring isobars, assuming isospin symmetry and therefore that the coulomb potential has a quadratic form [25].

Reaction Rate Calculation

Following Fisker in [21], we now consider the determination of the reaction rate based on nuclear structure information. For charged particle reactions, the specific reaction rate is given by

$$\langle \sigma v \rangle = \sqrt{\frac{8}{\pi \mu}} \frac{1}{(kT)^{3/2}} \int_0^\infty S(E) \exp\left(-\frac{E}{kT} - \frac{\sqrt{2\mu}\pi e^2 Z_1 Z_2}{\hbar E^{1/2}} \right) dE, \tag{2.3}$$

where E is the center-of-mass energy and μ is the reduced mass.

The nuclear physics is contained in the cross section σ, as defined in Equation 2.2.3 within the astrophysical S-factor

$$S(E) = \sigma(E) E e^{2\pi\eta(E)}, \tag{2.4}$$

where the Sommerfeld parameter is given by

$$\eta(E) = \frac{e^2}{\hbar} Z_1 Z_2 \sqrt{\frac{\mu}{2E}}. \tag{2.5}$$

The cross section is divided into two parts corresponding to direct-capture (to states below the proton separation energy in the compound nucleus) and resonant contributions (from states a finite distance above S_p, or in some cases broad sub-

threshold resonances), $\sigma = \sum \sigma_{res} + \sigma_{dc}$. The resonant capture cross section due to a single resonance is given by the Breit-Wigner formula,

$$\sigma_r(E) = \frac{\pi\hbar^2}{2\mu E}\frac{2J_r+1}{2(2J_T+1)}\frac{\Gamma_p\Gamma_\gamma}{(E-E_r)^2+(\Gamma/2)^2}, \tag{2.6}$$

here given specifically for radiative proton capture on a target nucleus with spin J_T to a resonance at energy E_r and with angular momentum J_r. Rigorously speaking, the widths Γ_p and Γ_γ are functions of energy, and the Breit-Wigner formula must be folded with the Maxwell-Boltzmann distribution and integrated over the relevant energy range to calculate the rate. For most practical purposes however, narrow resonances may be approximated as δ-functions with a particular constant value taken from the Maxwell-Boltzmann distribution to allow analytical integration for the reaction rate due to the single resonance [26],

$$\langle\sigma v\rangle_r = \left(\frac{2\pi}{\mu kT}\right)^{3/2}\hbar^2\omega\gamma\cdot\ \exp\left(-\frac{E_r}{kT}\right), \tag{2.7}$$

where $\omega\gamma$, the resonance strength, is given by

$$\omega\gamma = \frac{2J_r+1}{2(2J_T+1)}\frac{\Gamma_p\cdot\Gamma_\gamma}{\Gamma}, \tag{2.8}$$

and Γ is the sum of all the partial decay widths at the resonance energy. The influence of tails of higher energy broad resonances also can be significant, but in practice these are often included in the direct-capture portion of the S-factor.

The γ-width is determined by summing the partial γ-widths for decay from the resonant state to all lower states which lead eventually to the ground state. These widths depend strongly on the transition multipolarity and type (electric or magnetic), and therefore a determination of the excited states' angular momentum and parity is important in addition to an accurate knowledge of the excitation energy of the resonance state itself from which the resonance energy is determined ($E_r = E_{\rm ex}$

- $S_{\rm p}$). The proton width may be expanded as a product of the spectroscopic factor and the single particle width,

$$\Gamma_{\rm p}(E_{\rm r}) = C^2 S_{\rm p} \Gamma_{sp}(E_{\rm r}). \tag{2.9}$$

So to find the capture rates to systems with low level densities without direct measurement, it is necessary to know the excited state spectrum of the compound nucleus, the proton spectroscopic factors of the states, and the transition probabilities between them, as well as a reasonable estimation of the direct-capture cross-section. Which excited states will be involved in direct-capture, which will contribute to resonant processes, and the resonance energies of the super-threshold excited states will depend on the proton threshold, S_p. S_p comes from the mass difference between the target and compound nucleus. To take full advantage of the precision measurements of excited state energies such as those discussed in this work necessitates mass determinations with precision better than 1 part in 10^7. Also, the β-decay and electron-capture lifetimes of these nuclei must be known to determine the reaction flow.

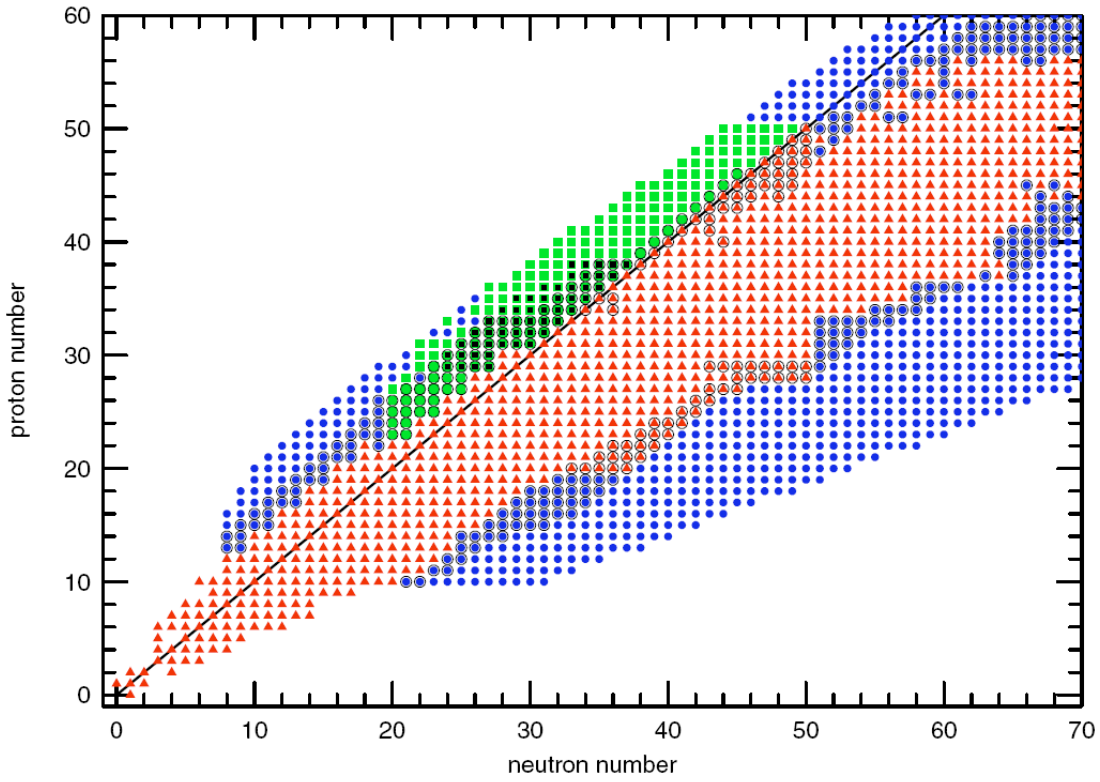

Figure 2.5: (Excerpted from [16], including internal references) Nuclear mass excesses taken from different data sources in the region of interest for the rp-process. A dark line shows the location of nuclei with Z = N. Red triangles indicate nuclei with experimentally determined mass excesses (Audi & Wapstra 1995). Nuclei with black circles surrounding a symbol indicate that an extrapolated or interpolated mass is available from Audi & Wapstra. For those circles enclosing a red triangle, these estimated values were used. Green squares, circled or not, show where data from Brown et al. (2002) and Brown (2002) was used. These add a calculated displacement energy to the Audi-Wapstra masses for N $\geq$ Z to obtain the masses of mirror nuclei with Z > N. For a subset of these (black squares inside green squares) from Brown et al. (2002), the errors in the calculated displacement energies are $\approx$ 100 keV. The solid green squares which cover a wider region are from Brown (2002) and have a larger error of several hundred keV in the calculated displacement energy due to the wider extrapolation and the possible effects of deformation in the A = 80 mass region. In the region of N = Z from A = 76–100, the error in the mass excess is dominated by the error in the Audi & Wapstra extrapolations, which are on the order of 0.5MeV. Finally, blue circles indicate mass excess data taken from Möller et al. (1995). These were used wherever shown, (circled or uncircled).

Chapter 3

Neutron Removal Experiment

3.1 Overview

Fortunately, much of the nuclear structure information needed for a more complete theoretical understanding of type I X-ray bursts can be obtained by experiment. As mentioned previously, direct measurements of resonant reaction rates in the Gamow window have been made on at least a few occasions (e.g. [20]), but even if a direct measurement is feasible, determination of the resonance parameters is sufficient to define the rate. Thus the effort required for a direct measurement is rarely warranted.

A relatively new method recently introduced by Clement et. al. [23, 27] uses neutron removal reactions with radioactive beams, whether by knockout or (p, d), to determine resonance properties (most importantly the excitation energy of the state) by detecting the γ-rays emitted from both sub-threshold and proton-unbound states in a nucleus ^{A-1}X, populated after the neutron-deficient nucleus ^{A}X undergoes neutron removal. More experiments of this type have now been successfully completed and are proposed for the future at the National Superconducting Cyclotron Laboratory (NSCL) among other laboratories.

The NSCL is one of the leading facilities in the world for the production of rare-isotope beams. The beams are produced by in-flight fragmentation of stable beams

at medium energies, such that the produced fragments have a high degree of forward focusing [28]. These fragments are then separated by the A1900 Spectrometer [29]. The A1900 consists of four dipoles and several focusing quadrupole triplets and higher order multipole elements which are capable of focusing and passing to experiments nearly all of a 5% momentum spread of fragments produced in the fragmentation target. Similar to other momentum-loss achromats, the A1900 separates fragments first by magnetic rigidity ($\chi_B = B\rho = p/q$, where B is magnetic field, ρ is bend radius, p is momentum and q is charge) then by momentum loss in a degrader located at a dispersive image in the middle of the system. It can be tuned to selectively pass any width up to it's maximum acceptance of these two parameters by cutting $B\rho$ at the system's center and cutting momentum-loss at its final focal plane.

From the fragment separator the in-flight separated rare-isotope beam is transferred to a reaction target at the target position of the S800 spectrograph [30]. The reaction target, chosen for large neutron removal cross-section, is surrounded by the highly-segmented germanium array SeGA [31]. As the nucleus ${}^{A}X$ undergoes neutron removal in the reaction target, it will selectively populate energy levels in the new nuclear system ${}^{A-1}X$. These levels typically decay on the femtosecond time-scale, well before the reaction product has left the target box. The decay γ-rays are then detected in SeGA and Doppler corrected based on their detection angle to determine the de-excitation energy to which they correspond in the nucleus ${}^{A-1}X$, preserving fine energy resolution.

The recoil nucleus ${}^{A-1}X$ proceeds out of the target box and is detected in the focal plane of the S800 Spectrograph, which is capable of energy resolution better than 1 part in 10^4. The detectors in the S800 focal plane allow the recoils to be identified with little uncertainty (see section 3.2.2), allowing the recoil to serve as a trigger for the data acquisition system to selectively record de-excitation γ-rays correlated with specific recoil nuclei.

Once the data is collected, the de-excitation energies evident in the spectrum of

the particular recoil nucleus being studied are assembled into a coherent excitation energy level scheme. Multiple coincident γ-rays (see Section 3.3.2) from a single recoil result from cascades and are used to place energy levels relative to each other as well as placing constraints on excited states' relative J^{π} values. The nuclei in this study are mirrors of well-studied neutron-rich isospin partners. Given the high degree of isospin symmetry, information from the excited state energies and decay branching ratios of the mirror nucleus can be used, together with theoretical shell model calculations, when drawing final conclusions as to the level structure. The first such experiment was a study of excited states in ^{33}Ar which successfully measured excitation energies with errors on the order of keV and reduced the uncertainty in the $^{32}Cl(p,\gamma)^{33}Ar$ reaction rate by three orders of magnitude [23].

Production rates of proton-rich nuclei decrease quickly toward the proton drip line. This is because projectile fragmentation is fundamentally a statistical process of nucleon removal, a process which must start with a stable or very long lived primary beam. This was the motivation behind the development of the neutron removal technique for studying proton rich nuclei. It takes advantage of the larger production cross-section for fragments with one neutron more than the isotope of interest, then produces the species to be studied in a subsequent reaction target. In this case, a polypropylene target will produce the species of interest both through (p,d) and through knockout on the C atoms. The other reaction channels populated, many of which produce previously studied nuclides, can be used to fix the position of the SeGA detectors relative to the reaction target.

The isotopes of interest in this study were ^{37}Ca and ^{36}K. A fragment beam of ^{38}Ca can be produced with a relatively high beam current from a primary beam of ^{40}Ca, since it only requires the removal of two neutrons from the beam. The angle of the momentum loss selection cut for this energy is such that the separator will select an isotonic series, so both ^{37}Ca and ^{36}K will be well populated in a single separator setting.

3.2 Experimental Setup

This experiment was performed at the coupled-cyclotron facility at the National Superconducting Cyclotron Laboratory. The primary beam was accelerated in the coupled K500 and K1200 cyclotrons, fragmented and separated in the A1900 fragment separator and passed through the transfer line to the S800 spectrometer in the S3 experimental vault. The isotopes to be studied were produced by reactions of the fragment beam in a target at the S800 pivot, surrounded by the Segmented Germanium Array (SeGA). The incoming fragment and the product of each reaction was identified unambiguously by a combination of time-of-flight measurements and the focal plane detectors of the S800. Coincident detection of γ-rays in SeGA allowed decay γ-ray spectroscopy of short lived nuclear excitations of each recoil isotope. Particular details of this process will be discussed in the following pages.

Probably better to mention specifically the detector suite here: the segmented CVD diamond timing detector, the segmented germanium array, the CRDCs, the IC and the S800 fp scint. Might ought to mention the diamond detector in the overview as well when comparing to previous experiments since it makes such a big difference here.

3.2.1 Fragment Production and Identification

A primary beam of $^{40}Ca^{20+}$ at 140 MeV/nucleon was produced in the coupled-cyclotrons and struck a 580 mg/cm^2 ^{9}Be foil at the target position of the A1900 fragment separator. The wide range of products from the production target were filtered first in the first half of the A1900 selecting a particular magnetic rigidity, which corresponds to a particular ratio of mass to charge, with a 0.5 % momentum width (dp/p) at the central dispersive image—Image 2—of the A1900. The close proximity of the primary beam to the fragment beam necessitated the use of a beam blocker at the exit of the first dipole. This reduced the acceptance of the fragment of interest by

some 10 % as observed at the focal plane of the spectrometer. Further separation was accomplished in the second half of the A1900 after momentum loss in a 238 mg/cm^2 achromatic Al degrader placed at Image 2. This separated the remaining products according to momentum loss, allowing a series of isotones through the 8 mm gap in the A1900 focal plane slits. All products were fully stripped bare nuclei. The dominant constituents in the cocktail beam at this point in the system were ^{38}Ca (61%), ^{37}K (28%), ^{36}Ar (10%), and ^{35}Cl (1%), which together made up approximately 97.5% of the total beam when measured at the extended focal plane of the A1900. The full cocktail was transported to the S3 vault with 98% transmission to the S800 object, measured by comparing rates on the CVD diamond detector at the S800 object and the scintillator at the extended focal plane of the A1900. Transmission of ^{38}Ca from the S800 object to the S800 focal plane was approximately 77%.

The component of the fragment beam responsible for each event was identified by velocity selection using two times of flight. Both time of flight (ToF) measurements took their start signal from the plastic scintillator in the S800 focal plane. The RF ToF was measured relative to a stop signal from the accelerating radio frequency in the cyclotrons and is therefore subject to uncertainty of the RF pulse width. This stop signal was downscaled by a factor of two from the RF clock in order to allow the full range of flight times to be recorded without a break at the RF period. The object ToF took the solid state diamond detector as its stop signal.

If there were no reaction target in the S800, the incoming fragments would be separable by either one of these two ToF measurements, but the velocity change do to energy loss and reactions in the target will spread the products of all fragments broadly in velocity, such that no individual ToF signal can separate them, as can be demonstrated clearly by imagining a projection of the data in Figure 3.1 onto either axis. Because the flight-times both include the full flightpath of the recoil nucleus—from the reaction target to the S800 focal plane—the ToF values for a product from a particular incoming fragment will be shifted by the same amount in RF ToF and in

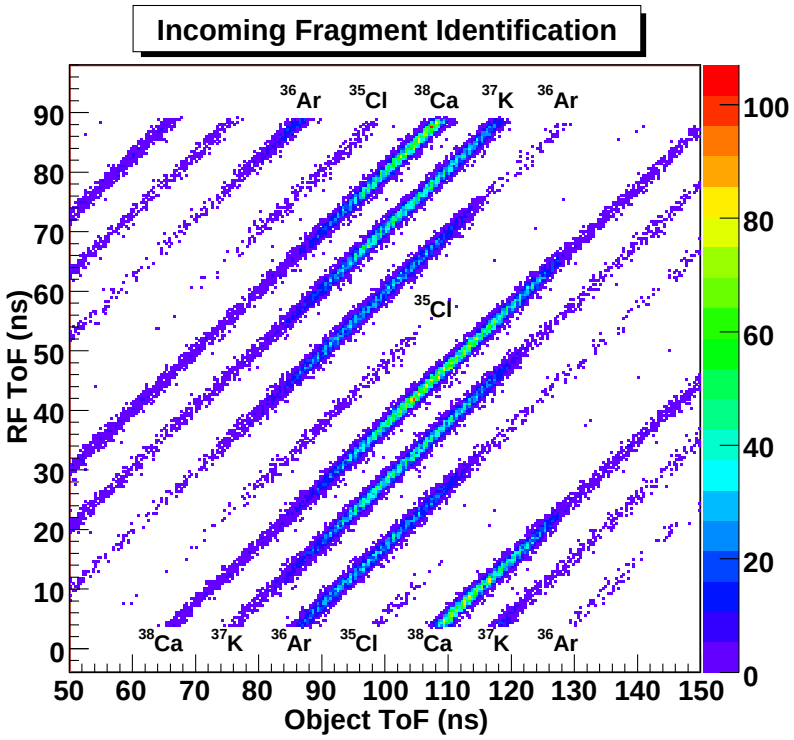

Figure 3.1: The relationship between the times-of-flight over the two flight paths are distinct for products of each of the four fragment beam components. The repeated vertical structure is due to the downscaling of the RF timing signal by a factor of two. The top and most intense band in each set of four corresponds to ^{38}Ca events, as labelled. Each band of events corresponds to the same fragment as in the similar structure at the top of the figure.

Object ToF relative to the expected flight times of the degraded fragment, so as to lie along a diagonal line of slope unity in the 2D spectrum through the expected position of the degraded fragment. The separation of these bands depends on a significant difference between the ratios $\mathrm{R}_{frag} = \mathrm{ToF}_{obj}/\mathrm{ToF}_{RF}$ of the degraded cocktail beam components. This separation is satisfied for this experiment because of the significant difference in the length of the two flightpaths.

Take for example, two distinct particle velocities, v_1 and v_2, over two distinct flightpaths, d_s and d_l. The ratio of the two flight times for a given particle (assuming a constant velocity over the flightpath) do not depend on the velocity of the particle but rather on the ratio of the lengths of the flightpaths.

$$t_{1l} = d_l/v_1 \qquad t_{1s} = d_s/v_1 \qquad t_{1l}/t_{1s} = d_l/d_s$$

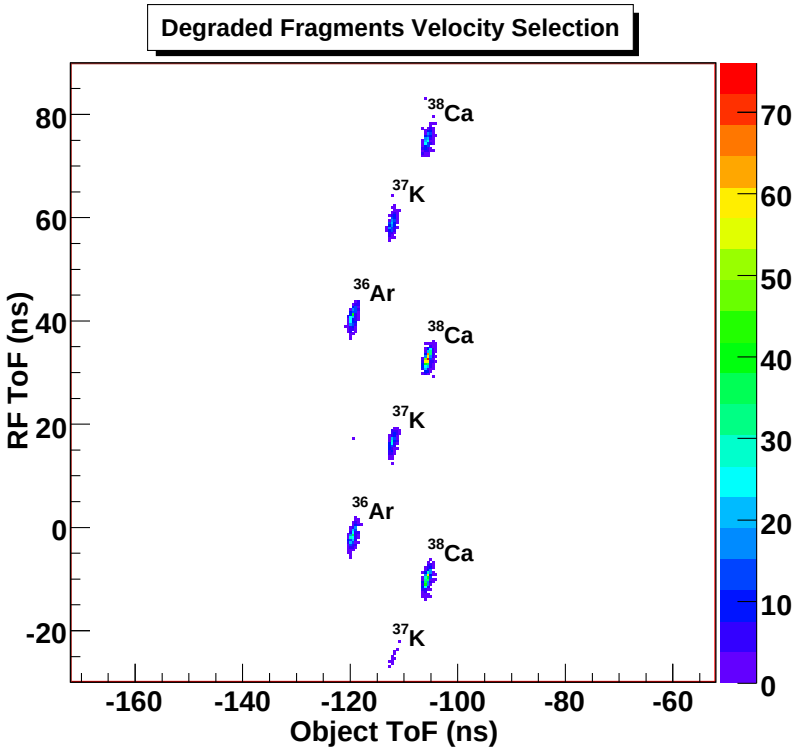

Figure 3.2: The RF ToF plotted against the Object ToF as in Figure 3.1 but in this case showing only events where the outgoing fragment is the same as the incoming fragment. The scale is the same on both axes to clearly show the slope in the degraded fragments due to the different lengths of the RF ToF and Object ToF flight paths.

$$t_{2l} = d_l/v_2 \qquad t_{2s} = d_s/v_2 \qquad t_{2l}/t_{2s} = d_l/d_s$$

So for two flightpaths of equal length, particles of all velocities would fall along a line of slope unity, which would confound any attempt to use the velocity selection discussed above. In this experiment $d_{RF} \approx 2.6 \times d_{Obj}$, and the degraded fragments in the cocktail beam—not so different from the constant velocity approximation considered in the above example—fall along a line in the RF ToF vs. Object ToF plot with a slope roughly equal to this ratio (see Figure 3.2), leaving each band of products (with slope unity) from a single beam component clearly separated from its neighbors.

Unambiguous recoil particle identification depends on this identification of the incoming fragment as will be seen in the following section.

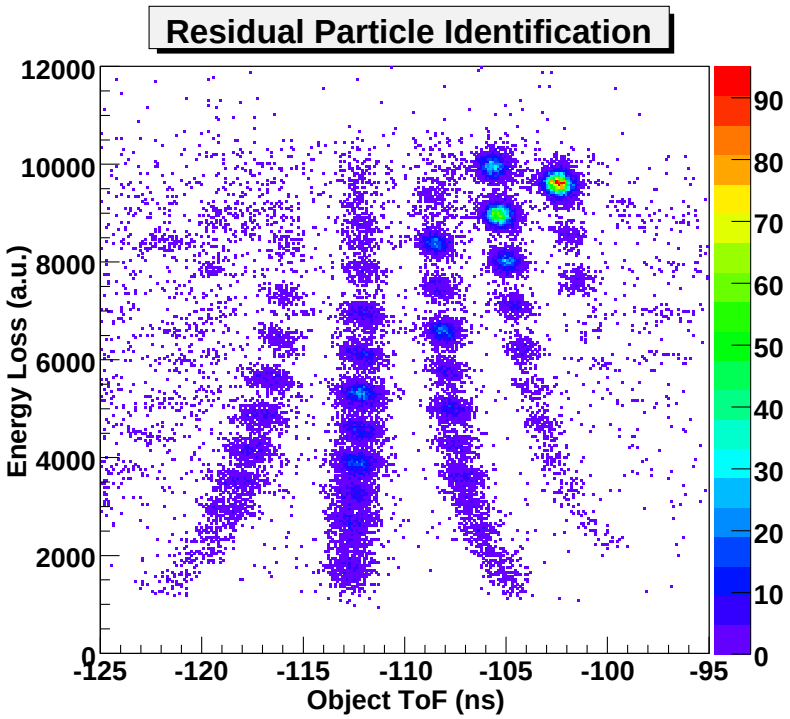

Figure 3.3: Products of incoming ^{38}Ca fragments are shown, plotting energy loss in the ionization chamber in the S800 focal plane against the ToF through the S800. ^{37}Ca is the most intense product, with ^{38}Ca located just to its upper left.

3.2.2 Residual Particle Identification

A 180 mg/cm^2 polypropylene reaction target was located in the target position of the S800, approximately 1.7 cm upstream from the pivot point. Numerous reaction channels were populated from each component of the incoming fragment beam, producing residual nuclei of numerous species on the chart of isotopes between the incoming fragment and the proton. Many of these are within the acceptance of the S800 and the sensitivity of the focal plane detectors. They can be identified in a plot of energy loss vs. ToF. Such a plot separates isotopes by charge and mass, for a limited acceptance of magnetic rigidity (B$\rho = p/q$). The energy loss separates by charge, since energy loss scales with the square of the charge while Bρ scales linearly with the charge, and ToF separates by mass-to-charge ratio, since a fixed Bρ requires $v \propto q/(m\gamma)$, where we use the relativistic definition for the momentum $p = mv\gamma$.

To improve the resolution of the particle identification plot, and thereby increase

the statistics and selectivity of the gated γ-ray spectra, the quantities plotted had some adjustments applied to remove some of the broadening due to the finite phase space of the particle beam. Note that the corrections to time of flight were only applied to the object time of flight and only that used for residual particle identification, not for the identification of the incoming fragment.

Inverse mapping the S800 in COSY [32] from information provided by the focal plane detectors allowed the calculation of the after target value for δ_K, the kinetic energy deviation from the central kinetic energy value—that which lies along the optic axis of the system. This kinetic energy deviation contributes to the width of the energy loss and object time of flight used in the particle identification, so linear corrections, tuned especially for ^{37}Ca residuals, were applied to both. Because only the upper photomultiplier tube was used as the start for the time of flight measurements, there is also some dependence of the time of flight on the x position in the S800 focal plane. This correction was not fit or applied separately. Rather it is assumed to be included in the correction based on δ_K, as this quantity is so strongly correlated with the x position in the focal plane.

The particle angle in the focal plane of the spectrometer, particularly in the dispersive plane, influences the length of the flightpath and therefore the time of flight. So the object time of flight was also adjusted linearly with the particle angle measured in the focal plane.

3.2.3 γ-ray Detection

The Segmented Germanium Array (SeGA) was placed about the reaction target in the standard configuration with a ring of detectors at roughly 90 degrees and another, more 'forward,' ring at roughly 37 degrees, both measured relative to the downstream optic axis. For this experiment we had nine detectors in the 90 degree ring and seven in the forward ring. Each roughly cylindrical SeGA detector is 32-fold segmented into four azimuthal sections by eight cylindrical slices. They are each positioned about

the target with their cylindrical axes roughly orthogonal to both a radial vector from the target and a circle about the beam axis connecting the detectors in a given ring (see Figure 3.4). In this configuration the angular resolution for Doppler correction is provided by the eight slices which are separated by roughly 40 mrad.

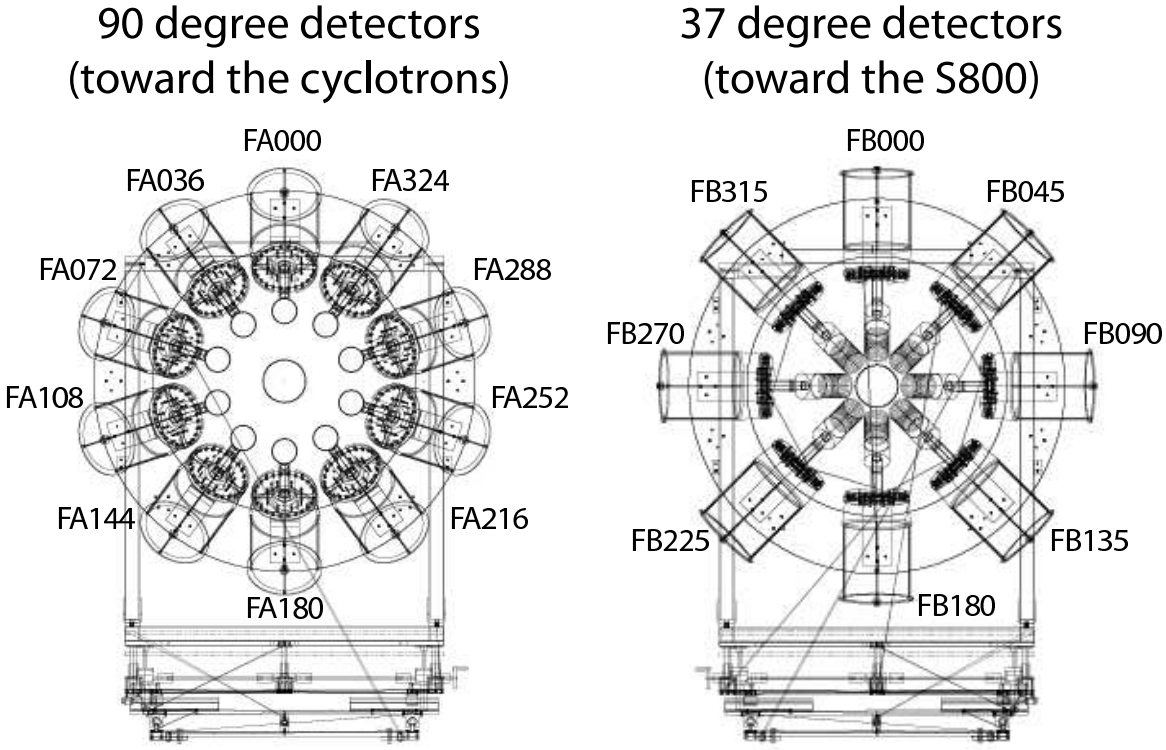

Figure 3.4: The SeGA detectors were arranged in classic configuration for this experiment with a total of 16 detectors, seven in the forward ring and nine in the 90^o ring. The circle in the center of each diagram is the beam pipe. Just outside the beam pipe are the cylindrical germanium crystals of SeGA. The larger cylinders near the edge of each diagram are the liquid N_2 dewars. Shown in this diagram is the full complement of 18 detectors.

We define a right-handed coordinate system for these detectors with the positive z axis pointing downstream from the target and the positive x axis pointing up (i.e. opposite gravity). The Doppler correction depends on the angle θ, between the recoil particle trajectory and the emitted γ-ray, and the velocity of the particle in units of c, $\beta = v/c$. This determines the ratio between the energy of the γ-ray in the rest frame of the recoil nucleus from which it was emitted and the energy observed in the

lab frame by the detectors.

$$E_{recoil} = \gamma E_{lab}(1 - \beta cos(\theta)), \tag{3.1}$$

where γ is the relativistic factor

$$\gamma = 1/\sqrt{(}1 - \beta^2). \tag{3.2}$$

In the analysis of this experiment, $cos(\theta)$ was calculated directly from the vector dot product between the position of the slice in SeGA where the γ-ray was detected and the direction of motion of the outgoing particle—whose direction immediately after the target was calculated in an inverse mapping of the S800—both taken relative to the center of the target.

The geometric position resolution for an emitted γ-ray given by the slices is not necessarily realized in events of higher multiplicity. A single γ-ray event will often involve interactions in more than one segment. In such cases the first segment hit determines the true angle for the Doppler correction. In this experiment, the first segment hit is assumed to be the segment with the largest energy deposited. This is true a majority of the time, but not always [33].

3.3 Analysis

The analysis was performed in the object-oriented data analysis framework ROOT [34] after converting the event files to root TTree files [35]. The advantage of using ROOT over SpecTcl 2.0 was a reduction in the time required to process the full set of events from over a week to approximately three hours. This atypically large processing time is due to the comparatively large number of events in this experiment whose production fragment is only two neutrons away from the primary beam. The experimental setup was novel in its use of the diamond timing detector and so the analysis code

from previous experiments of this type was not usable, instead a new code was written to be run by CINT, the C/C++ interpreter incorporated into ROOT. This code also abandoned the use of the PROCESS loop structure in favor of a more flexible user defined looping over the events [36].

3.3.1 Detector Calibration and Gating

The incoming fragment identification gates, discussed above in Section 3.2.1, were defined on the raw Object ToF vs. RF ToF spectrum, since no correction was required to achieve the necessary resolution. Changes in the delay timing used for the ToF signals from the diamond timing detector at the Object position early in the experiment require that two sets of gates be defined for fragment identification, one before and one after the timing shift.

Position and angle information were needed in the S800 focal plane to allow inverse mapping of the beam particles to the reaction target position. Two cathode readout drift chambers (CRDCs) provided this information.These detectors are based on ionization of a gas within the detector volume by the traversing heavy ion particles. A potential gradient within the detector causes the charge created to drift and be collected on the pads of the segmented cathode. The distribution of the charge on the pads determines the position in the dispersive direction (x) and the drift time determines the y position.

Variations in the collection efficiency and amplification of the pads require the addition of fitted offset values, called pedestals, to the signal of each pad, so that the centroid of the deposited charge across several pads in any given event will accurately represent the position of the particle. The x and y position in each detector were calibrated, based on the pad centroid and drift time TAC, using specially designed removable masks built into the S800 focal plane box for this purpose. Fluctuations in the properties of the detector over time, primarily in the gas, will change the calibration, so mask runs for position calibrations were performed every 12 hours for

both CRDCs through the course of the experiment.

As discussed above in Section 3.2.2, the identification of the residual particle detected in the S800 focal plane was done by the standard energy loss verses ToF method. The energy loss in the ionization chamber in the S800 focal plane for any particular recoil isotope has a significant finite width contribution from the energy spread of the recoils. This contribution can be eliminated using the S800 inverse mapping to reconstruct the energy deviation, δ_k, and making a linear adjustment to the measured energy loss.This improves the resolution of the particle identification.

Similarly, the Object ToF for a given recoil isotope is broadened both by the momentum spread and the angular deviation from the optic axis. These are corrected linearly based on the reconstructed δ_k and the angular deviation in the dispersive direction, measured in the focal plane. In this case there are four unique slopes for each of the two corrections, one for each segment of the diamond timing detector.

The individual recoil nuclei are clearly resolved in the ΔE-ToF particle identification (PID) spectrum—with one PID spectrum from each fragment beam component—even more so after applying the corrections discussed above. PID gates for the recoil nuclei of greatest interest were drawn by gating the ΔE-ToF spectrum on prominent γ-ray lines produced by each nucleus. This method was used for ^{37}Ca (first excited state), ^{36}K (800 keV line), and ^{38}Ca (2213 keV line). ^{38}Ca is not a focus of this study, but neighbors ^{37}Ca and ^{36}K and is a possible contaminant of both in the recoil PID spectrum from incoming ^{38}Ca fragments. A preliminary Doppler correction of the γ-rays detected in SeGA was used for these γ-ray gated analyses, since the final determination of the detector positions and recoil velocities were only determined later based on analyses of particle gated γ-ray spectra. Other PID gates were drawn manually. As in the case of the fragment identification gates, there were two sets of PID gates defined, one before and one after the delay change to the Object timing detector.

The lab frame energy calibration of the 16 SeGA detectors was performed using

^{226}Ra and ^{152}Eu sources as well as room background radiation. A total of 44 calibration lines were used: 23 from a ^{226}Ra source, 11 from a ^{152}Eu source, and 10 from room background radiation, including the highest energy calibration point at 2614.5 keV. These points were used to produce a bi-linear energy calibration, consisting of two independent linear calibrations above and below 1050 keV. Higher energy lines were present, e.g. at 3053.9 keV and 3081.7 keV in ^{226}Ra, but not sufficiently populated to be used in the calibration. This contributes some uncertainty to the measured energies above 2600 keV whose energy calibration is therefore an extrapolation.

Comparing source runs at the beginning and end of the experiment revealed a significant shift in the energy calibration for all of the SeGA detectors, with especially large shifts in three detectors. The shift is equivalent to an energy shift of a 3 MeV γ-ray by approximately 14 keV for one detector in the forward ring and between 6 and 7 keV for two detectors in the 90^o ring. The remaining detectors have shifts of between 1.4 keV and 4.3 keV for a 3 MeV γ-ray. Calibration runs taken throughout the course of the experiment showed that the trend in the calibration coefficients was largely linear over time (cf. Figure 3.5). These same calibration runs were then used together with pre-experiment and post-experiment calibration runs to produce a bi-linear energy calibration that depends linearly on run number. So each of the four terms in the bi-linear energy calibration of each detector is calculated for each run from a constant term and a linear term multiplying the run number.

The time of the signal in the unsegmented central contact (CCT) of SeGA is recorded in the data stream and can be used as an additional selection criterion. The resolution of the time signal is poor because of the substantial shaping time of the analog signal, but it can still eliminate some γ-rays accidentally coincident with recoil particles.

The analysis included γ-ray events of all detector multiplicities. Eliminating events interacting in only a single segment in a given detector would eliminate a significant fraction of Compton scattering events, but the use of GEANT simulations for fit-

ting the summed spectra eliminates the need for the improved clarity generated by multiplicity gating, while allowing the full statistics to be used.

Typically the position of the segments within each of the SeGA detectors has been determined by a series of physical measurements using a theodolite. In this experiment however, there are sufficient statistics such that a calibration based on the detected γ-rays from well-known transitions determines the detector positions more precisely than the theodolite measurements. As has been done recently by others [37], the angles of each slice in the detector relative to the downstream beam axis are determined by fitting the centroids of certain Doppler shifted γ-lines, which are sufficiently populated to be fit with a Gaussian curve for each of eight slices of each of the 16 SeGA detectors. This does not fully determine the position of the SeGA detectors in three dimensional space, but with the additional specification of an azimuthal angle ϕ for each detector it does do so relative to the optic axis of the beam, which is all that is needed for Doppler reconstruction.

The fitting is performed using the TMinuit class of ROOT. The fit includes 19 parameters for SeGA and additional terms for each nucleus and transition used including:

- 16 polar angles θ, one for each detector, measured from the downstream beam axis;
- 2 dθ values giving the angle between slices, which is required to be the same for all detectors in the same ring;
- 1 dθ fraction for slice A, which defines the fraction of dθ to be applied for the slice on the endcap, whose effective center is shifted due to the broken cylindrical symmetry in the detector volume;
- 1 β defining the velocity of each fragment/residual combination used; and
- 1 energy for each γ line used, since some lines have significant uncertainties

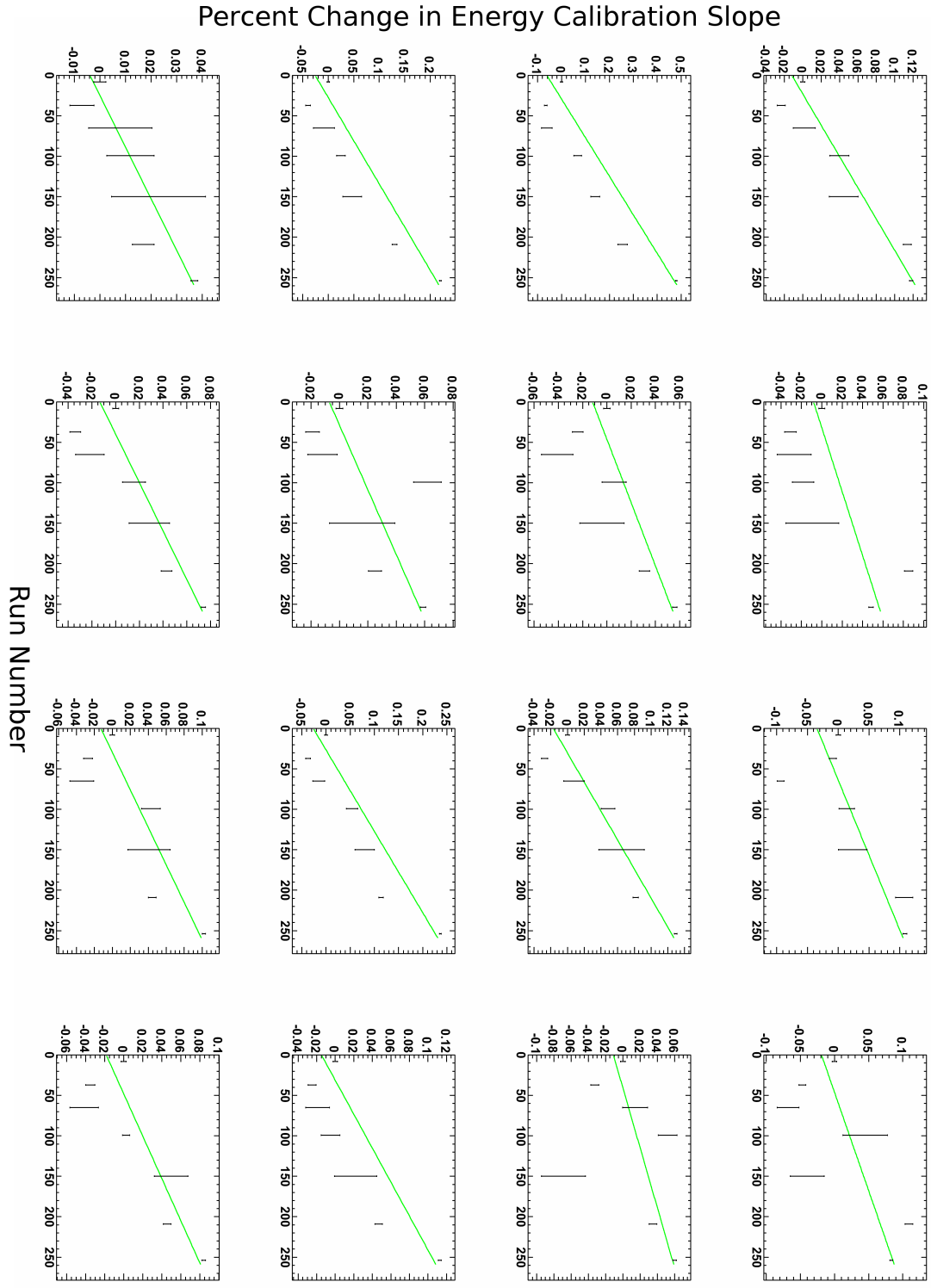

Figure 3.5: The shift in the linear energy calibration slope for energies above ≈ 1050 keV is plotted by detector for all calibration runs. The final high-energy slope in the bi-linear energy calibration is calculated for each run based on a linear fit to these values (green lines).

Many known lines were populated in this experiment and were considered for use when calibrating the detector positions. Useful calibration lines should satisfy several conditions. They must have a lifetime that is very short compared to the time for the particle to traverse the target thickness, roughly 6 ps in this experiment. Longer-lived states, or states fed by transitions from longer-lived states may decay after the target, which would indicate different angles. The transition must be very well populated to appear clearly in spectra for individual slices. The transition must be sufficiently isolated so that the fits will not be perturbed. Six lines were used in the final SeGA position calibration. They are listed in Table 3.1.

Table 3.1: In-flight decays used to calibrate SeGA detector positions. Lifetimes marked with an asterisk are unmeasured, so values have been taken from the analog state in the mirror nucleus.

Fragment	Recoil	E_γ (keV)	Lifetime (ps)	Binning (keV/chan)
^{38}Ca	^{37}Ca	1613 (17)	0.130*	8
^{38}Ca	^{35}Ar	1750.6 (3)	0.420*	20
^{38}Ca	^{34}Ar	2090.8 (3)	0.320 (40)	10
^{38}Ca	^{31}S	1248.8 (3)	0.500 (125)	10
^{37}K	^{35}Ar	1750.6 (3)	0.420*	16
^{37}K	^{34}Ar	2090.8 (3)	0.320 (40)	20

Energy calibrated, lab frame γ-ray spectra gated on each fragment/residual combination used in the SeGA position calibration were created and saved. Gaussian fits to the particular lines of interest in the lab frame were used to produce centroids and centroid errors for each line in each slice of the full array. The fitting routine used these lab frame energies by slice and determined the proper location of each slice of SeGA within the constraints of the framework discussed above.

Two corrections were necessary in the above process. The recoils were not all centered in the momentum acceptance of the S800. Consequently, the angular distribution at the target that would be accepted by the S800 varied by recoil. None were precisely on the optic axis, as calculated from an inverse mapping to the S800 target position from the focal plane detectors. A beam component with an angle off

of the optic axis at the S800 target used to determine the detector positions would produce an apparent shift in the detector angles, so the angle used in the Doppler correction when fitting each detector angle was corrected for the centroid of the angular distribution of each recoil nucleus. This ensures consistency both between the different recoils used in the position calibration and for the particle-by-particle angle corrections that will be used in the final analysis.

It is also necessary to correct in the detector position fitting for the discrepancy between the actual energy of an emitted γ-ray and the centroid of a simple Gaussian fit to the photopeak it generates in the Doppler corrected spectrum. This is because simple Gaussian fitting is used to determine the centroids of the lab frame lines to fit the detector positions, while fits to response functions from GEANT3 simulations of SeGA will be used to determine the energy of the states of interest. The discrepancies—generally on the order of 2 keV—were determined individually and corrections were applied for each of the lines used in the multi-recoil detector position fit. Residuals by detector and slice for the six calibration lines used are shown in Figure 3.6.

Calculating the inverse map of the S800 requires the specification of of z_{target}, the position of the target along the beamline relative to the S800 pivot, which cannot result from such a calibration alone. So as a first step, the position of the target and the beam spot on the target were adjusted iteratively relative to the SeGA detectors in positions determined by the theodolite measurements to best reproduce some calibration lines.

The velocity of ^{37}Ca recoils from ^{38}Ca fragments was determined by fitting GEANT3 simulations to the data for the first excited state decay line. The energy of the state was varied as a free parameter and the relative position of this transition in the two rings of SeGA determined the beam velocity. This gives an energy for the first excited state of ^{37}Ca at 1606.4 keV. The velocity of ^{36}K recoils from ^{37}K fragments was similarly determined using the previously unmeasured state now determined to be at

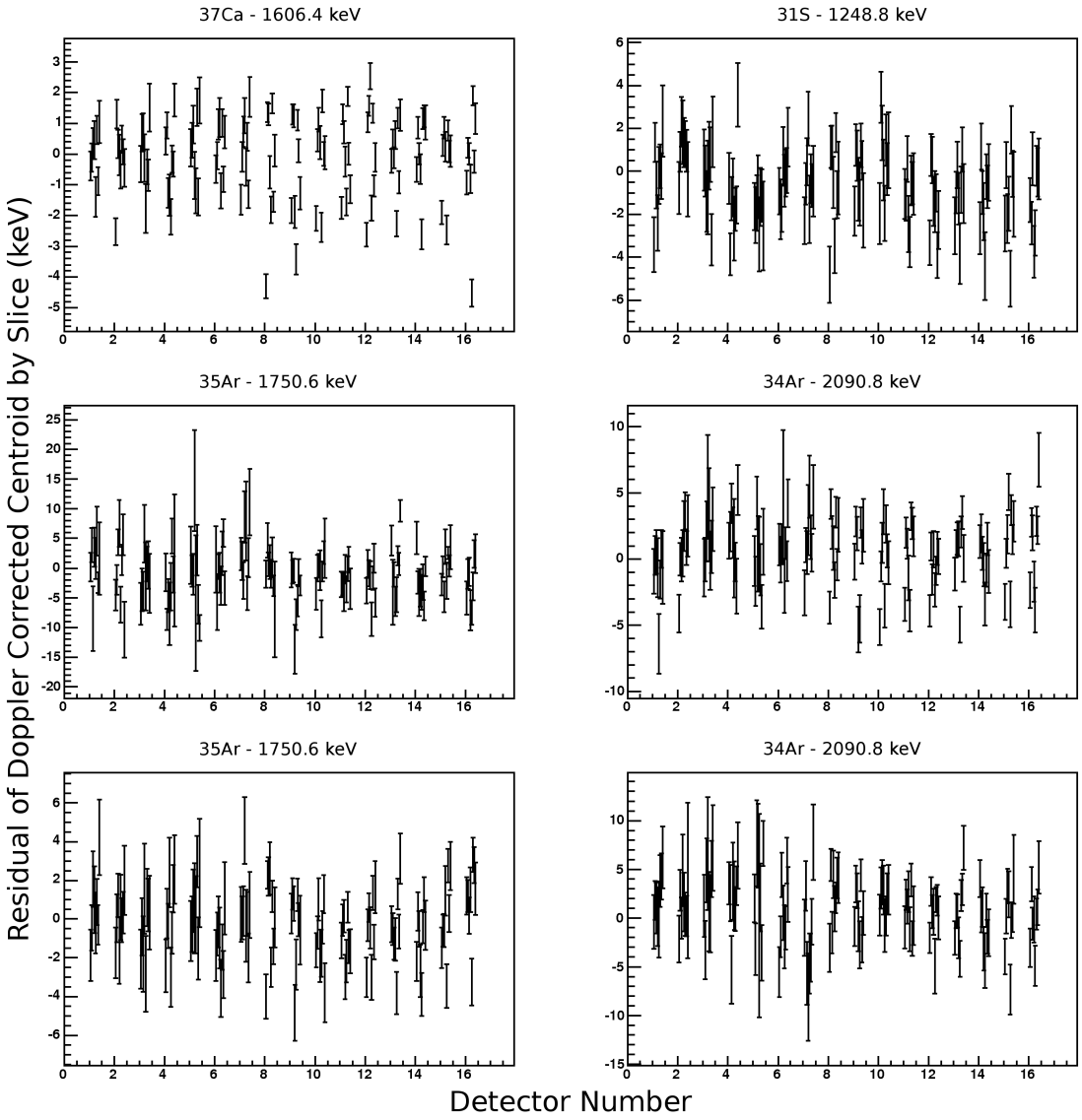

Figure 3.6: The residuals for each of the six calibration lines (separate plots) are shown by detector (x-axis) and slice (slightly offset). The topmost Ar isotopes are recoils from ^{38}Ca fragments and the lower Ar isotopes are recoils from ^{37}K fragments.

1916.2 keV. This calibration gives the known 1619.0 (2) keV state in agreement with the published value at 1618.91 keV.

3.3.2 γ-γ Coincidences

In addition to the two-particle, one-γ coincidences that form the bulk of the events in this study, we also consider two-particle, two-γ coincidences. The coincident γ-rays in

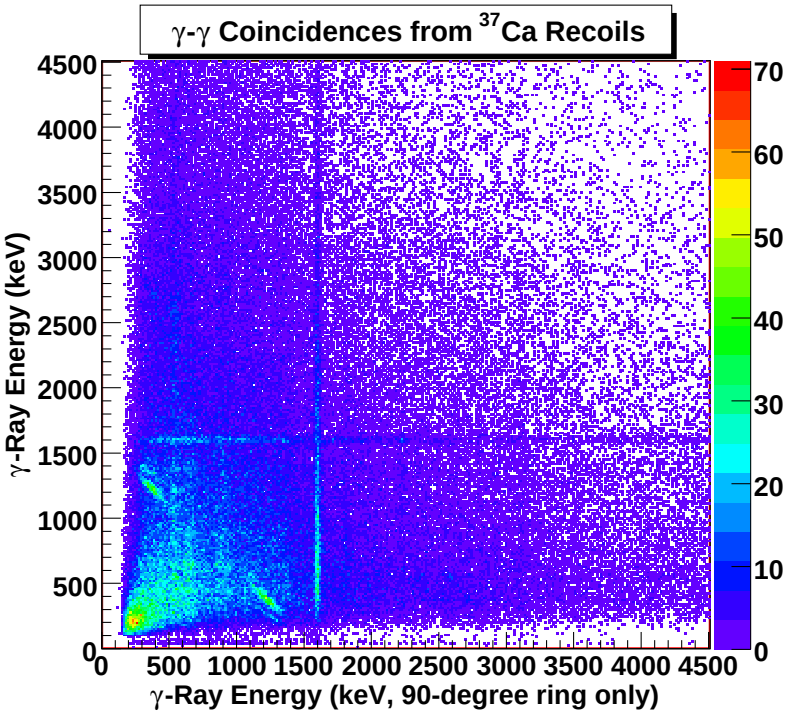

Figure 3.7: The hybrid γ-γ coincidence matrix from ^{37}Ca recoils. Only energies from events in the 90^o ring are plotted on the x-axis, thus all events shown include at least one interaction in the 90^o ring of SeGA detectors.

these events, together with information from the mirror nucleus, give insight into the relative placement of the observed transition lines into the excited state structure of the recoil isotope of interest. In this analysis a 2-dimensional histogram is constructed, correlated with a particular recoil isotope and a particular incoming fragment, with events plotted at the intersection of the two coincident γ-ray energies. Because of the total efficiency of SeGA, on the order of 0.01%, the rate of these higher detector multiplicity events will be orders of magnitude lower than single detector events. Since SeGA is not Compton suppressed, a significant amount of Compton scattered photons will appear in the coincidence matrix. For example, Compton scattered photons from the first excited state decay of ^{37}Ca can be easily observed in the sample coincidence matrix (Figure 3.7) as a diagonal structure along a line from (0,1606) to (1606,0).

Table 3.2: The expected energy levels above S_p in ^{37}Ca based on the structure of ^{37}Cl and the average Coulomb shifts observed in A = 37 $T_z = \pm 1/2$.

E_x (MeV)	E_r (MeV)	J^π_n	Γ_p (eV)	Γ_γ (eV)	$\omega\gamma$ (eV)	γ-branch	C^2S ν
3.09	0.07	$5/2^+$	2.06×10^{-21}	2.44×10^{-2}	1.23×10^{-21}	1.0	0.05
3.50	0.48	$5/2^-$	2.09×10^{-2}	3.13×10^{-2}	7.54×10^{-3}	0.60	0.002
3.63	0.61	$3/2^+$	5.98×10^{-3}	2.12×10^{-2}	1.87×10^{-3}	0.78	0.06
3.71	0.69	$3/2^+$	2.44×10^{-2}	1.46×10^{-2}	3.66×10^{-3}	0.38	0.06
3.77	0.75	$9/2^-$	3.02×10^{-2}	2.86×10^{-5}	2.86×10^{-5}	9.39×10^{-4}	0.002
4.02	1.00	$3/2^+$	3.29	6.58×10^{-3}	2.63×10^{-3}	1.99×10^{-3}	0.06

3.3.3 Deduced Structure and Resonances in ^{37}Ca

The proton separation energy (S_p) for ^{37}Ca is 3025 (24) keV [38, 39]. The states of interest in *rp*-process burning are those above and within approximately 1 MeV of S_p, as discussed in Section 2.2.3. Only the ground state and first excited state—well below S_p at 1613 (17) keV [39]—have been experimentally measured previously. The ^{36}K(p,γ)^{37}Ca reaction rate was previously based on excitation energies taken directly from the mirror nucleus ^{37}Cl [19]. Our expectations follow similarly, taking positive parity states' energies directly from the mirror but reducing the energy of negative parity states, which have shown significant Coulomb shifts in nearby nuclei, by 240 keV. This is the average value of the Coulomb shifts observed in negative parity states between ^{37}Ar and ^{37}K. The expected properties of excited states above the proton threshold are listed in Table 3.2 [40]. Spectroscopic factors were calculated for the $5/2^+$ state, which was the only obvious sd-shell state above the proton threshold, while the other states' spectroscopic factors and γ-widths were estimated [40]. The $7/2^-$ state in ^{37}Cl at 3103.5 keV is naturally not shown, since it's predicted position at 2864 keV, based on these assumptions, is well below threshold. Resonant capture to the $5/2^+$ state at roughly 3090 keV would be inhibited by low penetrability. The three succeeding states would be the dominant contributors to the capture rate at burst temperatures (0.1 GK < T < 1.5 GK).

We infer from the isospin mirror, ^{37}Cl, the likely γ-decay branchings of the excited

states of interest [38] and therefore the lines that they will populate in the observed spectrum. The three $3/2^+$ states are all expected to have significant branching both directly to the ground state and through the first excited state. The highest energy $3/2^+$ state also should have a branch through the $5/2^+$ state, and the $9/2^-$ state is expected to have significant branching both to the ground state and through the $7/2^-$ state. The $5/2^+$ and $5/2^-$ states, together with the $7/2^-$ state not shown in Table 3.2, are all expected to decay almost exclusively directly to the ground state. The small neutron spectroscopic factors estimated for the negative parity states suggest that they are unlikely to be observed in this study. The $9/2^-$ and $7/2^-$ states are the only two states in the mirror with lifetimes appreciable by this experiment, at 15 ps and 23 ps respectively, these lifetimes would produce observable discrepancies in the Doppler corrected energy of the line between the forward and 90^o rings in SeGA.

The first excited state is observed at 1606.4 keV (see Figure 3.8) consistent with the previous measurement [39]. The structure above the proton threshold is surprising, however. The transitions observed in this experiment and level assignments are shown in Figure 4.1. Here they will be discussed in order of decreasing clarity of spin and parity.

A strong line at 2230 keV (see Figure 3.9) coincident with the first excited state decay (see Figure 3.10), together with a peak at 3842 keV, suggest this as one of the three astrophysically important $3/2^+$ states, with a strong branch through the first excited state. This is the only decay to the first excited state strong enough to be observed clearly in the particle-gated γ-singles spectrum.

The line observed at 3103.7 keV is shifted in energy between the two rings of SeGA and also has a high energy shoulder in the forward ring spectrum, both of which indicate an appreciable lifetime, $t_{1/2}$ greater than a few picoseconds. Based on the structure of the mirror, the most reasonable assignment for this transition would be as the $7/2^-$ state decay to the ground state. The energy is higher than expected at roughly the same energy as the mirror state, but the only other state expected

to exhibit such a lifetime, the $9/2^-$ state, would have to drop by roughly 900 keV from the mirror and is not expected to be observed based on it's small estimated spectroscopic factor.

The transition observed at 2939 keV is first assumed to be the $5/2^+$ state because of it's location. This would represent a drop of roughly 150 keV from the mirror, particularly unexpected for this sd-shell state (see Section 4.1.1). The lowest expected $3/2^+$ state would have to drop by roughly 700 keV. On the contrary, the possible coincidence with the first excited state just above 1300 keV would seem to imply that this state may in fact be a dramatically shifted $3/2^+$ level.

The line at 3354 keV falls in what was expected to be a 490 keV gap in the spectrum. A possible coincidence with the first excited state observed at roughly 1750 keV suggests that this may be one of the three astrophysically important $3/2^+$ states. Also, the expected energy levels were calculated without considering that one of the $3/2^+$ states results from a 2 particle excitation to the $f_{7/2}$ shell, which would be expected to drop in energy toward the drip line (see Section 4.1.1). This level could also possibly be the $5/2^-$, the closest expected state, roughly 400 keV higher in the mirror, though it is not expected to be so strongly populated.

The two nearby ground state transitions at 3530 keV and 3612 keV may both have some feeding through the first excited state, based on the structure in the coincident spectrum just above and below 2000keV. The coincidences are somewhat vague however and so these two levels could be either two $3/2^+$ states or one $3/2^+$ and the $5/2^-$.

3.3.4 Deduced Structure and Resonances in ^{36}K

For ^{36}K S_p is 1666 keV [38]. As before, the states of interest are those above S_p. Of particular interest are the three states whose resonant capture contributions are expected to dominate the proton capture rate at burst temperatures: a 2^+ state at 1890 keV, a 3^- state at 2270 keV, and a 2^+ state at 2410 keV [41]. The first of these,

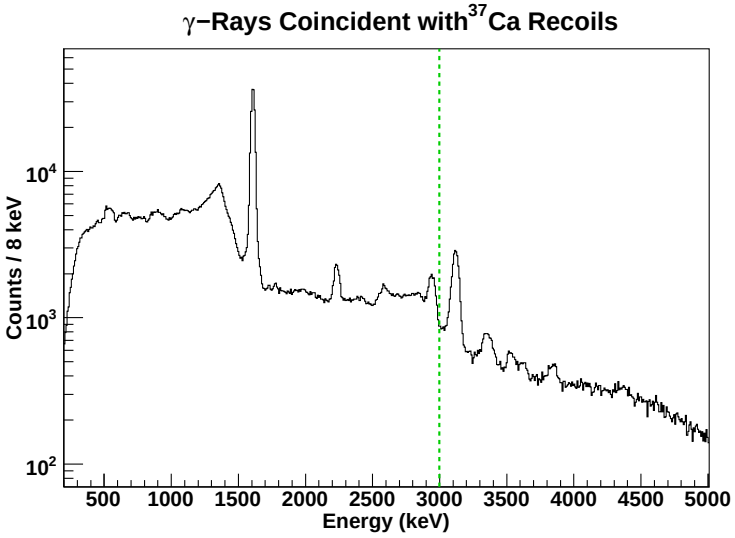

Figure 3.8: γ-rays observed in SeGA in coincidence with ^{37}Ca recoils in the S800. The proton separation energy is marked by the green dotted line at 2998.4 (2.0) keV.

Table 3.3: The expected energy levels above S_p in ^{36}K.

E_x (MeV)	E_r (MeV)	J^π_n	Γ_p (eV)	Γ_γ (eV)	$\omega\gamma$ (eV)	γ-branch	C^2S ν
1.89	0.22	2^+	2.49×10^{-7}	6.76×10^{-3}	1.56×10^{-7}	1.0	0.72
2.27	0.60	3^-	1.21×10^{-1}	2.46×10^{-4}	2.31×10^{-4}	2.2×10^{-3}	0.09
2.41	0.74	2^+	6.79	1.34×10^{-2}	8.39×10^{-3}	2.0×10^{-3}	0.34

which is expected to dominate the capture rate up to approximately 0.6 GK, is the only one expected to decay primarily through the γ branch, to which this experiment is sensitive. The other two states are predicted to decay primarily by proton emission with $\Gamma_\gamma < 0.01 \times \Gamma_p$ in both cases. This makes their observation challenging.

We infer from the isospin mirror, ^{36}Cl, the likely gamma branchings of the excited states of interest [38] and therefore the lines that they will populate in the observed spectrum. The 1890 keV 2^+ state is the only state of these three expected to decay primarily to the ground state. The 3^- state is expected to decay through the first 2^- state, which is most likely the state observed in the spectrum (Figure 3.11) near 1700 keV. The higher energy 2^+ excited state is expected to decay primarily through the first 1^+ state, most likely that observed in the spectrum at 1112 keV.

The error in previous experiments is 20 keV or greater for all of the states of

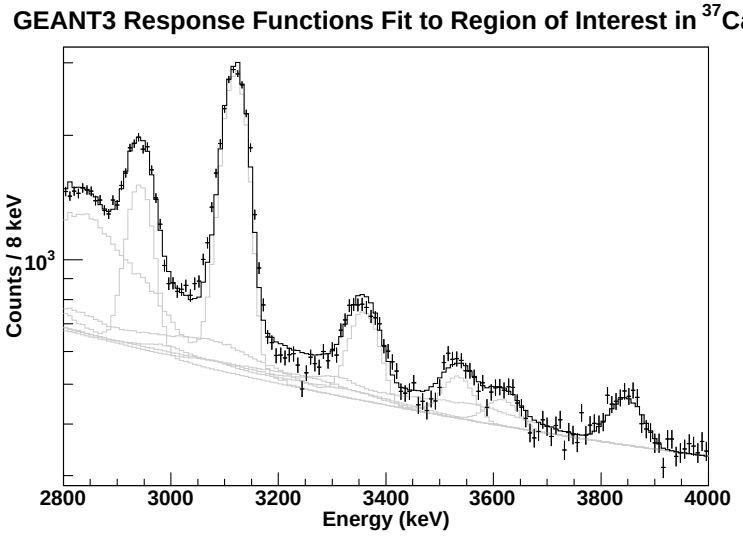

Figure 3.9: The data histogram from the 90^o ring in SeGA is shown as points with errors. The black curve is the fitted sum of GEANT response functions with an exponential background. Each individual response function is plotted in gray including the background.

interest [42]. Two lower energy states below S_p at 1112.8 (4) keV and 1619.0 (2) keV are better known [43]. The velocity of the recoils for the sake of Doppler correction is set by fitting the strong, isolated line just above 1900 keV in both rings of SeGA with response functions from GEANT3 simulations. Its parent state is expected to have a short lifetime which is consistent with the peak shape. The two states immediately above the proton threshold were the focus of this experiment. Measurement of the energies of the lower states, specifically those with literature values of 1112.8 keV and 800 keV is complicated by lifetime effects.

The fit of GEANT3 response functions to the data histogram is shown in Figure 3.12. The three lines are fit at 1618.9 (14) keV, 1706 (28) keV, and 1916.4 (14) keV respectively. The transition observed at 1706 keV is assumed to be the direct transition to the ground state of the 1670 (20) keV state identified in [42]. The 1916.38 keV transition is assumed to be the transition to the ground state of the state previously identified as 1890 (20) keV. These are both above the upper bound of the uncertainty in the previous measurement. No peak is observed at 560 keV where a transition from 2270 keV to the 1706 keV level would be expected, and the

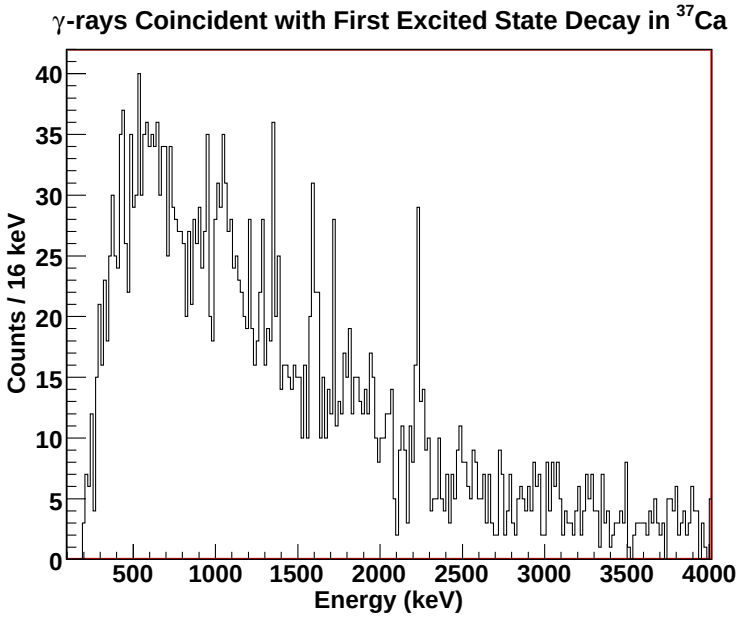

Figure 3.10: Shown are the γ-rays coincident with the decay of the first excited state in ^{37}Ca recoils.

2410 keV to 1112 keV transition is not observed. So we have no observation of either the 2270 keV state or the 2410 keV state.

3.3.5 Deduced Structure and Resonances in ^{36}Ca

^{36}Ca has been the subject of recent interest both for it's possible influence on *rp*-process burning [44] and as a probe of shell structure far from stability. While it was not the focus of this study, it is populated as an exit channel of incoming ^{37}Ca fragments and was within the acceptance of the S800. Approximately 40,000 γ-rays were correlated with ^{36}Ca recoils. The spectrum from the 90^o ring is shown in Figure 3.13. The proton separation energy is 2560 (40) keV [38]. The sole resonance participating in *rp*-process burning is the first excited state, a 2^+ state, which has been measured at GSI at 3015 (16) keV in [45] and at GANIL at 3036 (11) keV in [46].

There are no other states observed in ^{36}Ca in this experiment, so the velocity of the recoils for the sake of Doppler correction is set by fitting the only observed transition in both rings of SeGA with response functions from GEANT3 simulations.

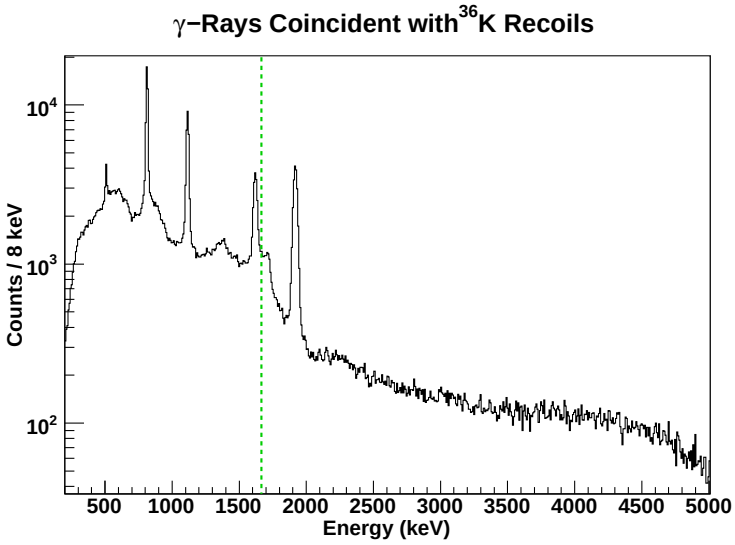

Figure 3.11: γ-rays observed in the 90 degree ring of SeGA in coincidence with ^{36}K recoils in the S800 from incoming ^{37}K fragments. The proton separation energy is marked with the green dashed line.

This determination should be accurate since the 2^+ state of interest is expected to have a very short lifetime, $t_{1/2} = 75$ fs in the mirror, which is much smaller than the time necessary to traverse the reaction target. The peak shape in both rings is also consistent with a short lifetime. The response function fit places the first excited state at 3045 keV (See Figure 3.14). The statistical error in the fit is approximately 1 keV. The error due to the velocity determination is conservatively estimated to be 1.7 keV. Combining these with the uncertainty due to the energy calibration and detector position fit gives a total error of 2.4 keV.

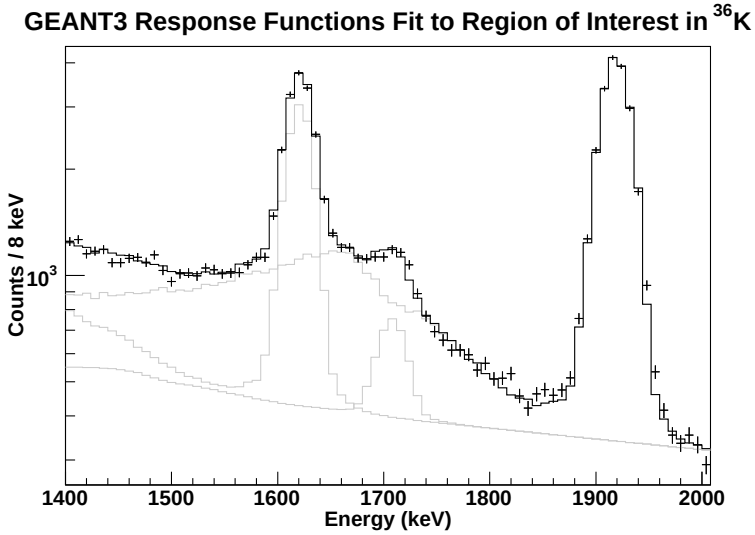

Figure 3.12: The data histogram from the 90^o ring in SeGA is shown as points with errors. The black curve is the fitted sum of GEANT response functions with an exponential background. Each individual response function is plotted in gray including the background.

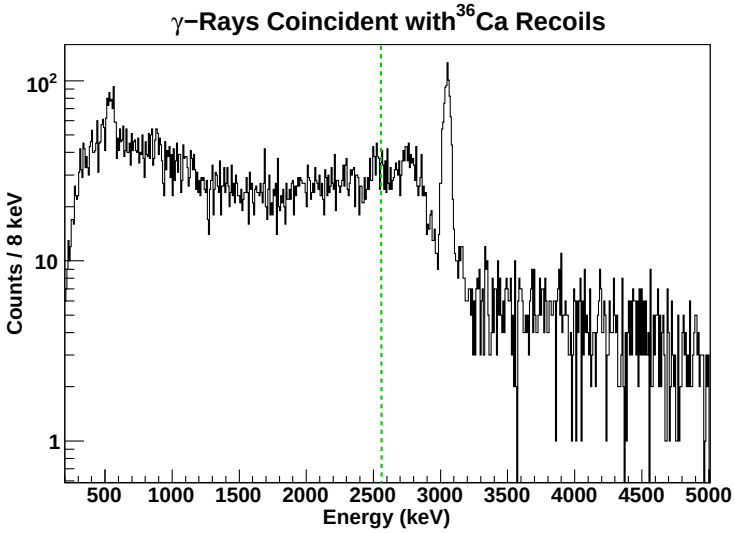

Figure 3.13: γ-rays observed in the 90^o ring of SeGA in coincidence with ^{36}Ca recoils in the S800 from incoming ^{38}Ca fragments. The proton separation energy is marked with the green dashed line.

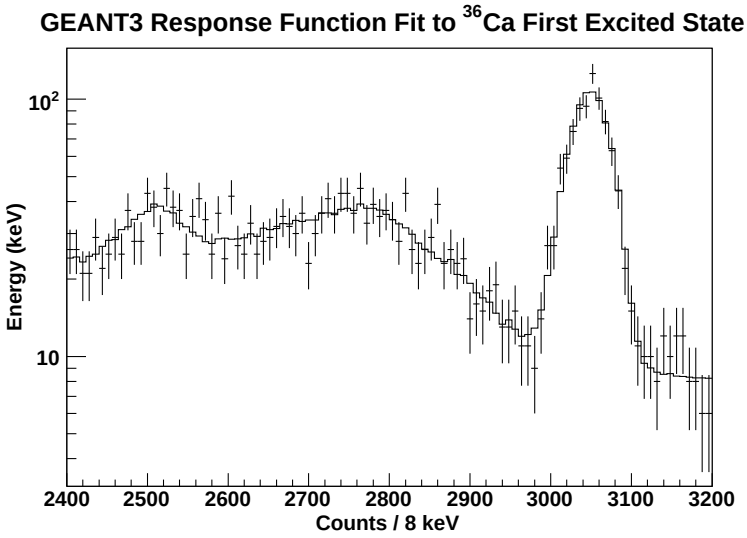

Figure 3.14: The data histogram from the 90^o ring in SeGA is shown as points with errors and the fitted curve is the line. A fitted exponential background curve has been added to the simulated response function.

Chapter 4

Results and Implications

4.1 Level Structure of ^{37}Ca

The level diagram showing the levels and transitions observed in this study is shown in Figure 4.1. A graphical comparison to the mirror states given in Figure 4.2. The implications of these new values within the framework of the nuclear shell model, the Isobaric Mass Multiplet Equation, and in explosive astrophysical burning scenarios will be discussed in the following sections.

4.1.1 sd-shell Calculations

There are currently no shell-model calculations available for ^{37}Ca that include the full sd- and fp-shell spaces, though recent calculations for nearby nuclei along A = 35 and A = 39 have successfully used the reduced valence space $s_{1/2}d_{3/2}f_{7/2}p_{3/2}$ [47]. Still, we can gain some insight from sd-shell model calculations. Calculations by B. A. Brown in the sd-shell suggest that one of the 3/2+ states is a product of population of the fp-shell. In the single-particle view this could be produced by promoting two neutrons to the $f_{7/2}$ shell from the $d_{3/2}$ shell. The resulting 3/2+ state would be expected to undergo the same downward shift, when compared to states in the mirror nucleus, due to the shrinking of the major shell gap between $d_{3/2}$ and $f_{7/2}$ single particle levels.

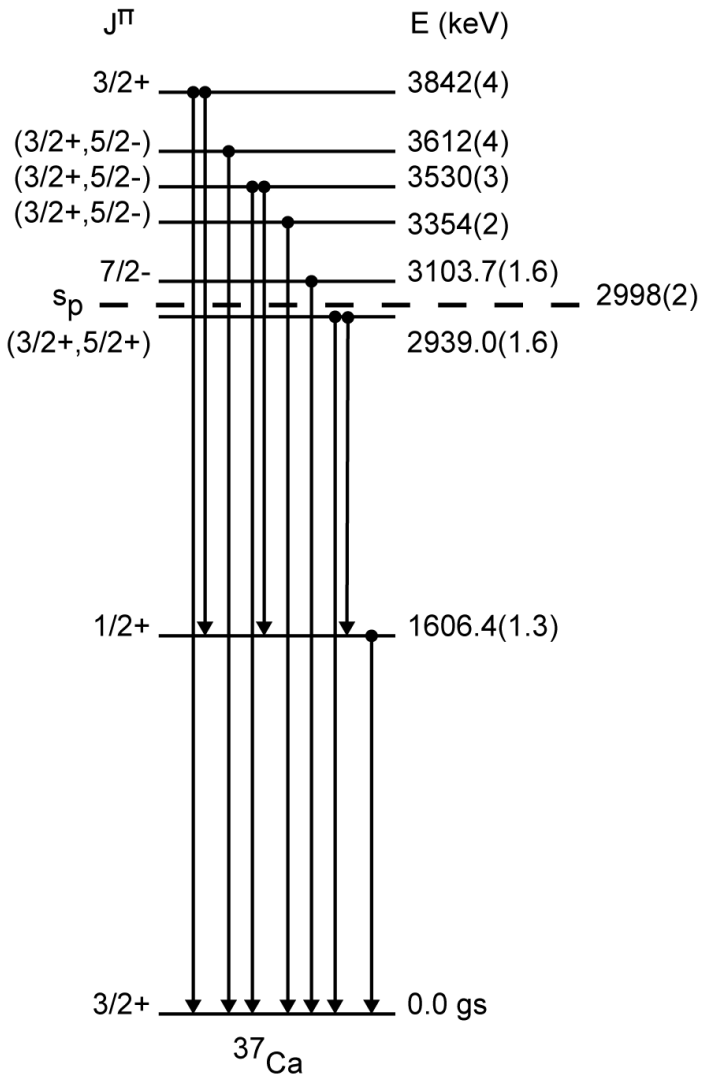

Figure 4.1: Excited states and transitions observed in the experiment. Spins and parities are not measured, but rather are inferred based on the structure of the mirror nucleus, with the most tenuous inferences in parenthesis. The proton separation energy is marked by the dotted line.

4.1.2 Isobaric Multiplet Mass Equation

The isobaric multiplet mass equation (IMME) approximates the coulomb effects to binding of nuclear states along an isobar. The assumed isospin symmetric nuclear potential should be modified by a quadratic function of the isospin projection T_z, since this is the form of the coulomb potential. Higher order terms in T_z have been observed in some cases, and imply breaking of the isospin symmetry. See [25] for a review of isobaric quartets in the IMME and their use in testing for symmetry

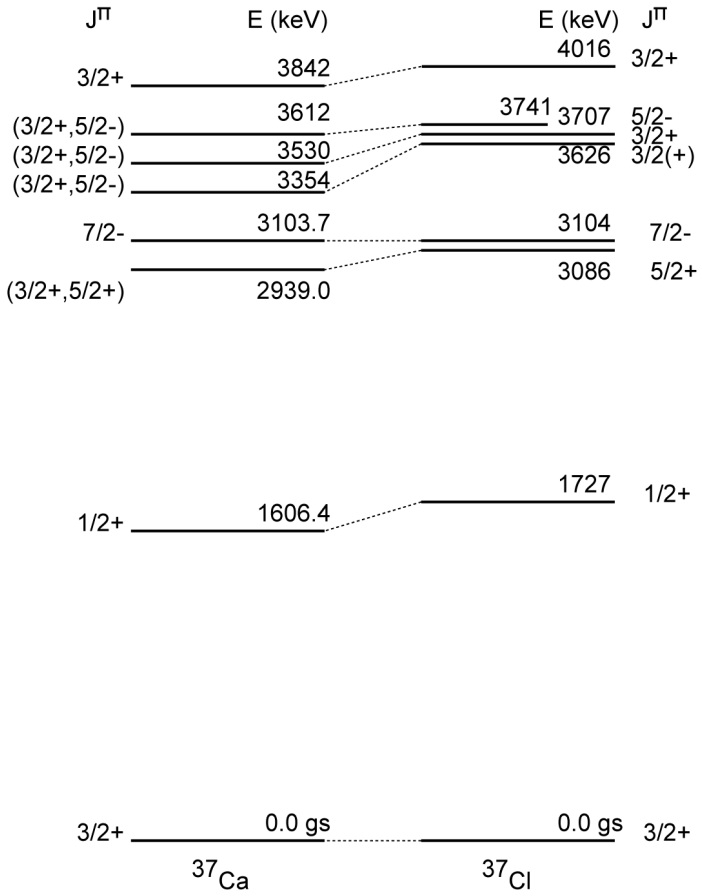

Figure 4.2: Measured excited state structure of ^{37}Ca compared with analog states in the mirror nucleus ^{37}Cl and transitions observed in the experiment. Spins and parities are not measured, but rather are inferred based on the structure of the mirror.

breaking.

A recent measurement of the mass of ^{37}Ca [48] has allowed the very precise determination of the cubic term (also referred to as 'd') of the ground-state quartet, placing zero outside the 1σ error bar. Without this improved mass measurement, the ground state mass uncertainty would greatly limit the utility of the precision measurements of this work within the IMME framework. For the first excited state in ^{37}Ca, the other three isobaric analog states in the quartet are also all known [38, 49]. The previous value for the first excited state in ^{37}Ca put zero just outside the 1σ error for the cubic term, with d = 0.0044 (41). The new value of 1606.4 (1.3) keV and the greatly reduced uncertainty have considerably increased the degree of extremity from zero, with d = $5.46\times10^{-3}\pm2.96\times10^{-3}$. Currently the uncertainty in the energy

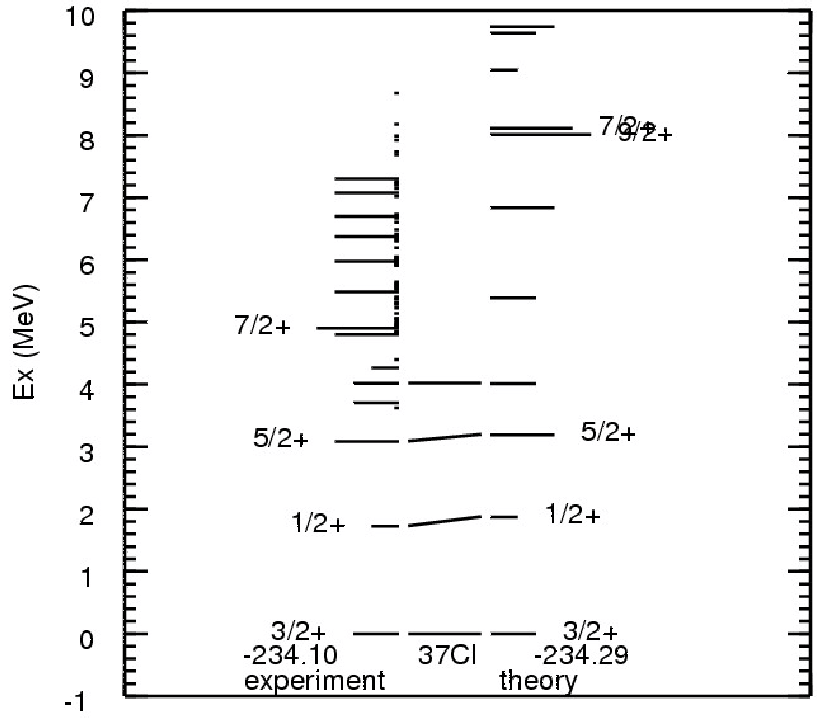

Figure 4.3: Sd-shell model calculations for ^{37}Cl show few sd-shell excited states in the region immediately above S_p except a single 5/2+ and one 3/2+ level.

of the $T_z = +1/2$ member of this multiplet, at 10 keV, is the greatest contributor to this error. More precise measurements of these states would clarify the extent of the asymmetry.

None of the higher T = 3/2 quartets are known completely as would be required to fit the cubic term in the IMME. Based on the inferred spin and parity of the $5/2^+$ state in ^{37}Ca at 2937.8 keV, a null value for the cubic term in the IMME would lead us to expect the unknown $T_z = +1/2$ level in ^{37}Ar at 8046 keV. Neither of the $T_z = \pm 1/2$ members of the quartet including the inferred $7/2^-$ state in ^{37}Ca at 3103.9 keV have been measured. Taking the linear and quadratic terms from the ground state quartet—the most precisely determined for A = 37—and further assuming a zero cubic term, we might expect the $T_z = +1/2$ level in ^{37}Ar at 8096 keV and the T_z = -1/2 level in ^{37}K at 8154 keV. Naturally these predictions should be taken with caution, since neither of the two fully measured quartets for A = 37 is consistent with a zero cubic term.

4.2 Astrophysical Implications

In ^{36}K the non-observation of the third and fourth excited states above the proton separation energy leaves the rate somewhat uncertain for higher temperatures, though the increase in energy of the dominant resonance at lower temperatures will increase the temperature at which it remains dominant above the previous 0.6 GK. Since this reaction rate is important primarily at earlier times and lower temperatures, this is likely the most important temperature region for which to constrain the reaction rate.

In ^{37}Ca the rate will be strongly enhanced by the considerably lower energy of the $3/2^+$ state at 3354 keV. This increases the reaction rate by 2–3 orders of magnitude for temperatures consistent with burst rise, between 0.2 and 0.4 GK. The new ^{36}K(p,γ)^{37}Ca reaction rate for burst temperatures is shown in Figure 4.5 together with the previously used rate. This increased rate leads to significant changes in the shape of the burst lightcurve produced in the multi-zone burst model KEPLER as can be seen in Figure **??**.

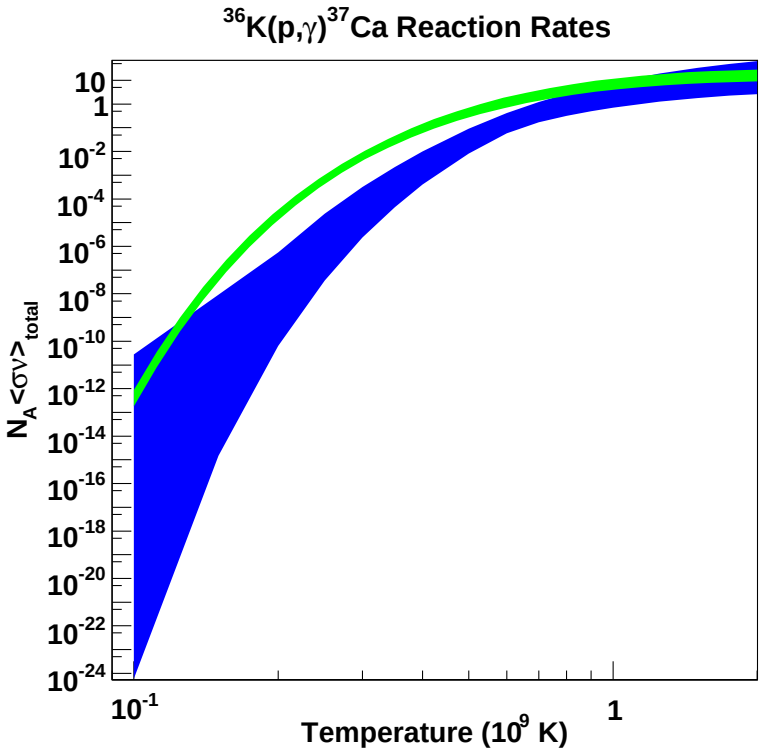

Figure 4.4: The new calculated reaction rate for ^{36}K(p,γ) based on the measurements in this work [green] over the previously estimated reaction rate [blue]. The uncertainty of the previous rate was estimated assuming a 100keV uncertainty in the excited state energies.

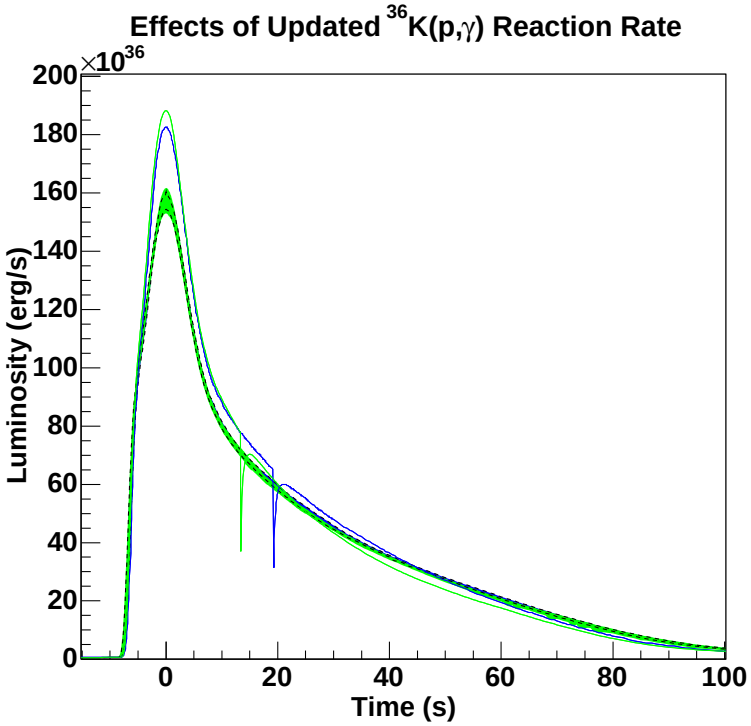

Figure 4.5: The effects of the updated ^{36}K(p,γ) reaction rate in the multi-zone burst model. Lightcurves with the updated reaction rates are plotted in blue and the baseline bursts in green. The first burst lightcurves are the two curves peaking at higher luminosity and the bands are the 1σ confidence intervals for a sequence of six bursts, modelling steady state bursting behavior. There is no change in the steady state bursting. The blue band, outlined by dashed curves throughout, is nearly completely covered by the green band. There is only a slight change in the lightcurve of the first burst, which is generally regarded as providing a cleaner rp-process, uncomplicated by the effects of compositional inertia.

Chapter 5

Study of Burst Sensitivity to (p,γ) and (α,p) Reaction Rates

5.1 Introduction

Burst model calculations are the bridge between the theoretical models of Type I X-ray bursts and observations, as briefly discussed previously in Chapter 2. They verify our theoretical understanding and explain the variety of bursting behavior as a function of the properties of the astrophysical system. Currently, models of these bursts are unconstrained due to the large uncertainties in the nuclear physics input to the *rp*- and αp-processes. Nuclear reaction rates, masses, excited state structure and weak decay properties determine the reaction pathway, energy generation, and final products of these events. These changes in the *rp*- and αp-processes result in observable changes in the X-ray bursts themselves in some cases.

The extent of these uncertainties is such that even those accessible to current experimental methods may not reasonably be addressed in their entirety. So experimental studies should be focused on the uncertain nuclear physics that result in the largest uncertainties in the observables. Previous studies looked at the bursts' sensitivity to large sets of rates varied all together (e.g. weak rates in the KEPLER

code [16]), multiple individual rate variations (e.g. (p,γ) rates in [50]), or large sets of rates each randomly varied simultaneously—known as the Monte Carlo approach (e.g. [51]).

This study focuses on the influence of individual uncertain (p,γ) and (α,p) reaction rates. The rates are first varied individually by a fairly generous constant factor up and down in the single-zone model of Schatz et al. [15]. Those rate variations to which the single-zone model observables show sensitivity were then varied in the multi-zone burst model, after first determining more realistic uncertainties based on the individual nucleus in question and the theoretical or experimental uncertainties present in the current estimate of the reaction rate. This hybrid approach allows both a comprehensive consideration of the full set of (p,γ) and (α,p) reactions involved in the process, by using the faster single-zone burst model, and a more complete consideration of those rates thought to be important in the fully coupled multi-zone model KEPLER.

While the single-zone model may not identify all the sensitive reaction rates that would appear in a comprehensive multi-zone study, it has shown the ability previously to identify some sensitivities present in the multi-zone model [50] and is a useful tool for such, until much more computing power is brought to bear to enable a comprehensive sensitivity study in a multi-zone model. As a further test, additional single-zone simulations using the reduced, realistic uncertainty used in the multi-zone model runs have shown rate sensitivities very similar to those observed in the multi-zone study.

The set of proton capture and (α,p) rates considered includes all those between the N = Z line and the proton drip line, 1697 rates total. An initial uncertainty of a factor of $100^{\pm 1}$ was used in the single-zone model for these rates. The Reaclib v1.0 rate library [52] was used for both the single-zone and the multi-zone codes to maximize consistency. Some rates are hard-coded in KEPLER and could not be updated. The 3α rate is taken from [53], which is within 10% of the updated rate

from [54] for all temperatures important to *rp*-process considerations (T between 0.1 and 2.0 GK). Some transfer reactions, such as (d,t), also are hard-coded, but should not be important either during or between bursts. So the rate libraries are functionally consistent.

Reaclib v1.0 is an expanded and updated reaction database based on the earlier reaclib200 [55], which was previously used in single-zone burst studies [50]. Reaclib v1.0 contains numerous updated rates from both theory and experiment when compared to the proprietary library previously used in KEPLER. New experimental masses [56] among other things have led to improved theory rates from NON-SMOKER calculations (to be discussed in [52]), replacing previous rates from Rauscher and Thielemann [57]. Nuclear structure and reaction experiments have led to updated reaction rates primarily for A ¡ 40. β-decay rates are updated to the latest compilation in [58]. These two libraries, in addition to the currently available rate library, Reaclib v0.5, are considered briefly as part of the multi-zone study in Section 5.4.

5.2 Realistic error estimates

There has been some disagreement in the literature about the level of uncertainty that should be used in sensitivity studies of this kind [50, 51]. We choose generous error estimates beyond 1σ error for two reasons. First, in many cases errors must be estimated based purely on the scatter of theoretical results, since there is no experimental data available to serve as their foundation. While this is understandable given the paucity of experimental data in many regions of the nuclear chart, it is not surprising that experiments often find reaction rates to be well beyond these error bounds, as was shown to be the case in the experimental study discussed in Chapter 3. Second, even correct 1σ uncertainties underpredict the error roughly one third of the time and therefore could conceivably miss (in the case of a non-linear dependence of burst observables on the rate), or at least underestimate (in the case of a linear

dependence of burst observables on the rate), fully one third of rate sensitivities. In either case, this type II error, or false negative, is the one to be chiefly avoided in sensitivity studies.

The much shorter list of reaction rate uncertainties that alter the observables substantially in the large-scale first step of the sensitivity study, assuming a large and uniform reaction rate uncertainty, may much more easily be given the careful consideration necessary to determine a realistic 2σ uncertainty as dictated by the current knowledge of the individual nucleus. This is why for our two step approach, we will adopt large error bounds of a factor of $100^{\pm 1}$ about the currently estimated rates in the first step in the single-zone model and roughly 2σ error for the rates of interest which are considered in the multi-zone model.

The upper and lower limits for reaction rate changes used in the multi-zone study depend on the specific case. For rates dominated by resonant capture, the new rates were calculated based on assumed 2σ uncertainties in the resonance energies (200keV for shell model calculated levels). Calculated values of partial widths, spectroscopic factors, etc. were used from [19, 21, 41] among others. For rates not dominated by resonant capture, or whose resonance energies are well known, the new rates were taken as constant factor multiples of the currently estimated rates based on the assumed rate uncertainty implied by the uncertain mass, spectroscopic factor, etc. as appropriate.

5.3 Single-zone simulations

The single-zone model was first "calibrated" to reproduce as closely as possible the lightcurve and ashes of the multi-zone code. Initial isotopic abundances were taken from several individual zones in the multi-zone model throughout the burst layer—the zones in which an initially significant mass fraction of H is almost totally consumed in the process of the burst—and each was processed in the single-zone model while

varying the initial temperature. The initial pressure was taken with the abundances from the same zone in the multi-zone hydrodynamics code. The abundances were taken from the multi-zone code at the time of the peak abundance of ^{15}O, which might be considered the point of *rp*-process breakout. The normalized lightcurve and final abundances produced by these single-zone burst models were then compared with those of the multi-zone code and the closest match was used as the initial temperature and composition for the single-zone sensitivity study. For these comparisons the single-zone lightcurve was normalized to match the peak luminosity of the multi-zone curve; hence only the shape of the single-zone lightcurve was considered. The initial temperature used was 0.386 GK.

The lightcurves produced using varied reaction rates were ranked according to the degree of change from the baseline Reaclib v1.0 lightcurve. Fairly few of the full list of rate changes produce large changes in the burst lightcurve. The lightcurves corresponding to reaction rates with the greatest sensitivity are shown in Figures 5.1 and 5.2. In the case of the (α,p) reactions, the tenth curve in dark green is already very nearly the same as that of the baseline rate library. The burst ashes (with isotopes summed by atomic mass) were also ranked according to the degree of change from the baseline burst. There was found to be a strong correlation between the sensitivity of the burst ashes and the sensitivity of the lightcurve to the individual (p,γ) reaction rates. The union of these two top 10 lists is shown in Table 5.1. The list contains only 12 reaction rates because only 2 reactions of the top to which the ashes were most sensitive were not also in the top ten lightcurve sensitivities.

5.4 Multi-zone simulations

The reaction rate variations to which the single-zone model showed the greatest sensitivity, together with other selected rates of possible interest (e.g. some mentioned in [51]), are considered in the multi-zone, one-dimensional Kepler model of Woosley,

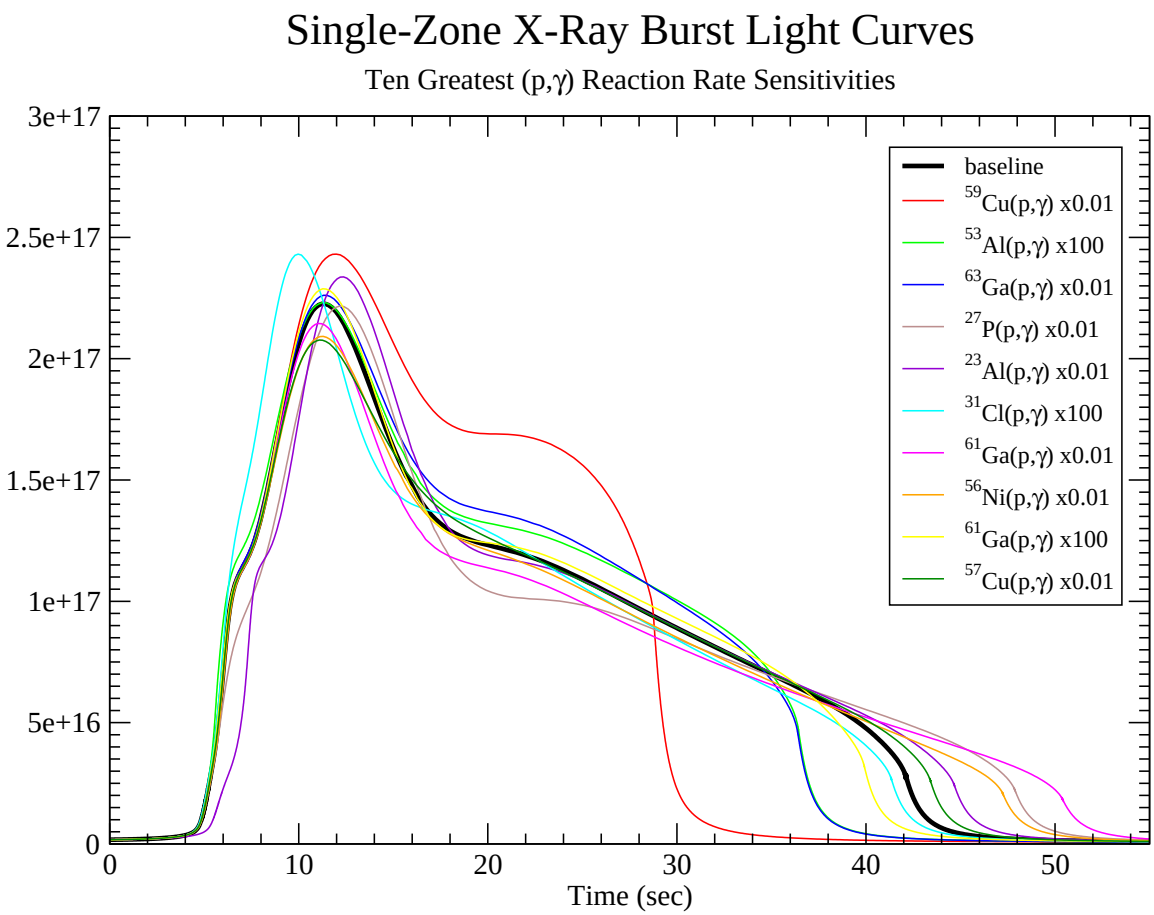

Figure 5.1: The ten most altered burst lightcurves from the single-zone sensitivity study of (p,γ) reaction rates are shown together with the baseline lightcurve generated using the standard Reaclib v1.0 reaction rate database to which they were compared.

Heger, et al. [16]. This model couples the energy generation of a complete, adaptive nuclear reaction network of over 1300 isotopes to a one-dimensional thermodynamic simulation of the accretion, subsumption, radiative energy and convective energy and mass transport both during and between bursts. This allows all of the consequences of steady state nuclear burning between bursts and compositional inertia throughout the surface layers from preceding thermal pulses to be included in long chains of bursts, with each burst igniting near the base of the hydrogen sea atop the ashes of the previous bursts and in the presence of the products of steady state burning.

The specific accretion model used for these studies is model ZM from [16]. This is accretion of solar metallicity material at a rate of 1.75 $\times 10^{-9} M_{\odot}$ per year (roughly 12% of the Eddington mass accretion rate). The neutron star is taken to be 10 km

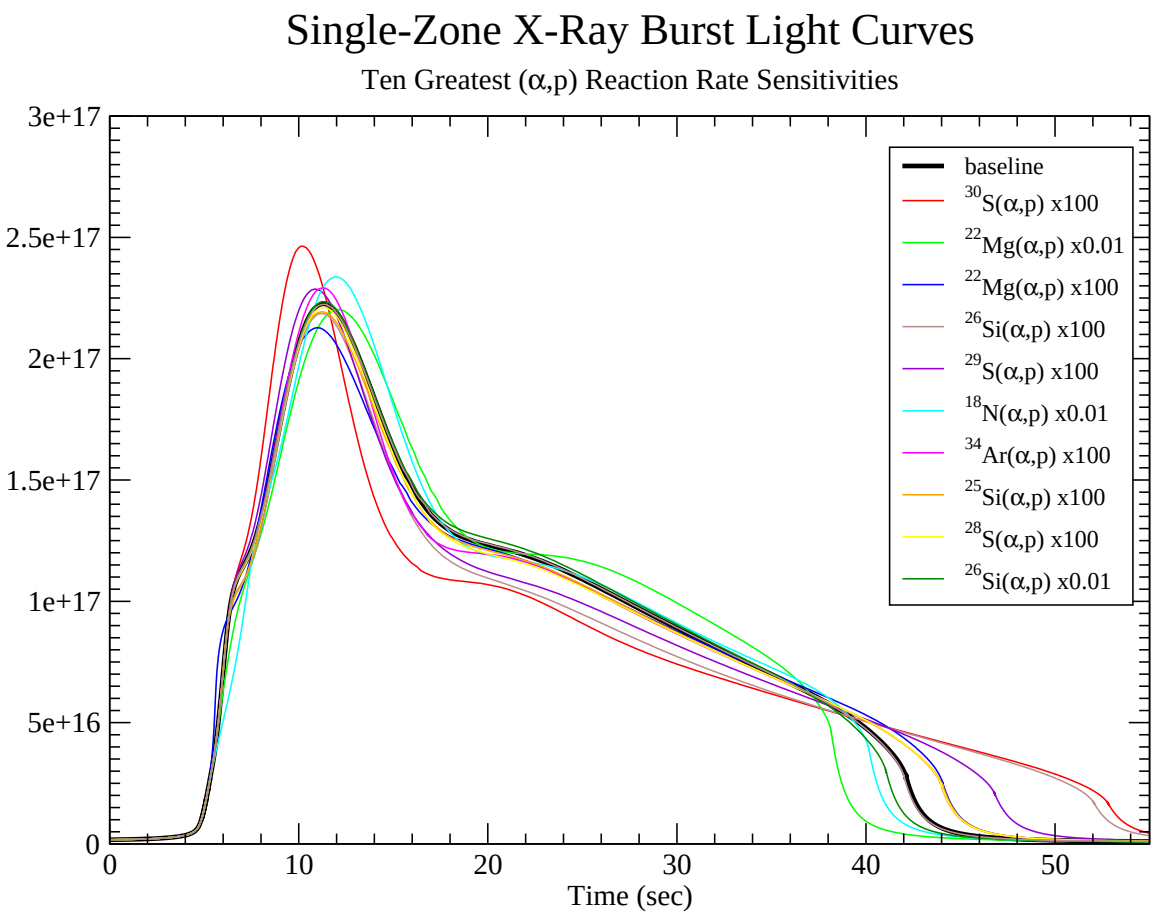

Figure 5.2: The ten most altered burst lightcurves from the single-zone sensitivity study of (α,p) reaction rates are shown together with the baseline lightcurve generated using the standard Reaclib v1.0 reaction rate database to which they were compared.

in radius and 1.4 solar masses. These same astrophysical model parameters were also used in model A4 in [17], where the resulting lightcurve and recurrence time compared favorably with bursts observed in GS 1826–24, a source discussed in more detail in [4]. Since this study compares model results to other model results, rather than to observations, we have not included relativistic corrections due to the deep gravitational well of the neutron star as were necessary in [17].

The model was first run for a long sequence of bursts using the new Reaclib v1.0 reaction rate database. The 1σ confidence interval luminosity band for 24 bursts is shown in Figure 5.3, compared to similar bands from extended simulations including 23 bursts using the Reaclib v0.5 database and 30 bursts from the proprietary reaction rate database previously used in KEPLER. These bands are constructed so as to

Table 5.1: The proton capture rates to which the single-zone burst model was sensitive, ranked in order of atomic number. The uncertainty used in subsequent multi-zone model calculations is given as a constant factor. For those marked with an asterisk, the assumed uncertainty of the resonance energies used to calculate a temperature dependent uncertainty is given.

Index	Reaction	Est. Uncertainty (factor)
1	^{23}Al(p,γ)^{24}Si	200keV*
2	^{27}P(p,γ)^{28}S	200keV*
3	^{31}Cl(p,γ)^{32}Ar	200keV*
4	^{35}K(p,γ)^{36}Ca	200keV*
5	^{39}Ca(p,γ)^{40}Sc	200keV*
6	^{40}Sc(p,γ)^{41}*Ti*	$3^{\pm 1}$
7	^{56}Ni(p,γ)^{57}Cu	200keV*
8	^{57}Cu(p,γ)^{58}*Zn*	200keV*
9	^{59}Cu(p,γ)^{60}Zn	$100^{\pm 1}$
10	^{61}Ga(p,γ)^{62}*Ge*	$3^{\pm 1}$
11	^{63}Ga(p,γ)^{64}Ge	$3^{\pm 1}$
12	^{65}As(p,γ)^{66}*Se*	$3^{\pm 1}$

Table 5.2: (α,p) rates to which the single-zone burst model was sensitive, ranked in order of atomic number. The uncertainty used in subsequent multi-zone model calculations is given as a constant factor.

Index	Reaction	Est. Uncertainty (factor)
1	^{18}Ne(α,p)	$30^{\pm 1}$
2	^{22}Mg(α,p)	$10^{\pm 1}$
3	^{25}Si(α,p)	$10^{\pm 1}$
4	^{26}Si(α,p)	$10^{\pm 1}$
5	^{29}S(α,p)	$10^{\pm 1}$
6	^{30}S(α,p)	$10^{\pm 1}$
7	^{34}Ar(α,p)	$10^{\pm 1}$

approximate steady state bursting behavior. To this end the first two bursts are excluded in all cases to avoid the effects of accretion to a bare ^{56}Ni surface (the first burst) and the first order compositional inertia from this accretion (the second burst). The remaining burst lightcurves are aligned with their peak luminosity at t = 0, and the luminosities are ranked at each point in time. The upper and lower one sixth of fluence values at each time are removed and the remaining maximum and minimum

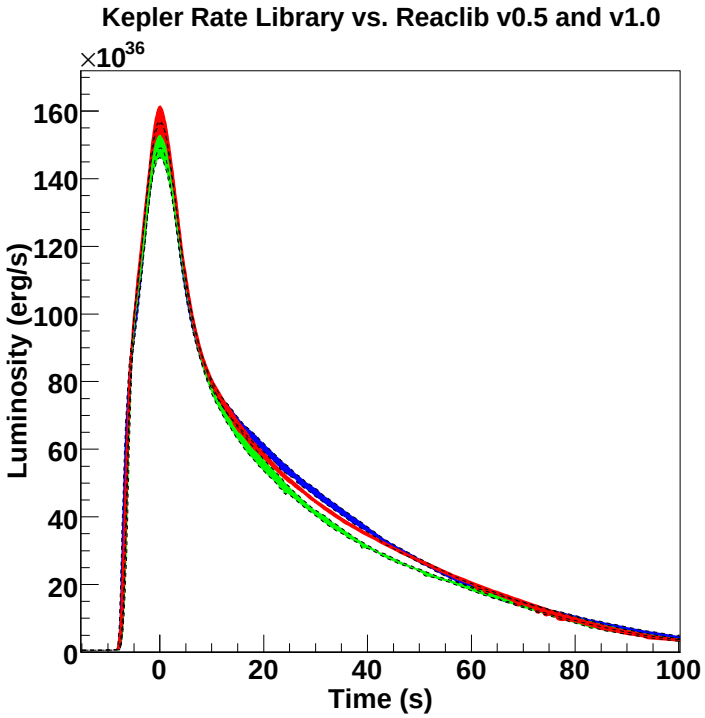

Figure 5.3: Multi-zone burst lightcurve 1σ confidence intervals are shown for different reaction rate libraries: the proprietary rate library of KEPLER [blue], the currently released Reaclib v0.5 [green], and soon to be released Reaclib v1.0 [red] which was used in this sensitivity study.

luminosities constitute the 1σ confidence interval. This method was chosen, instead of the RMS for example, because it does not depend on any assumed shape of the distribution of the luminosities, thus eliminating any possible skew due to extreme outliers. The only difference between Reaclib v1.0 and the proprietary KEPLER rate library were discussed in Section 5.1. Reaclib v0.5 is very similar to Reaclib v1.0 except that the new, unpublished NON-SMOKER reaction rates are not included.

The results of each rate variation are plotted similarly, comparing the lightcurve confidence intervals from simulations using the upper and lower limits of the rate uncertainty in each case. Each confidence interval includes four of six lightcurves run beyond the first two bursts. The first two bursts are excluded when constructing the confidence intervals, as before, in order to model steady state bursting behavior. Plots below show the most significant changes in steady state bursting behavior. While it

is not always easy to infer the particular cause of a given rate sensitivity, because of the complexity of the system, some possibilities will be mentioned briefly for a few cases.

The considerable sensitivity to the ^{23}Al(p,γ) reaction rate (see Figure 5.4) could easily be seen as a consequence of the very low proton separation energy of ^{23}Al, S_p = 125 (25) keV). This would lead to a very low equilibrium abundance of ^{23}Al at the high temperatures present during burst ignition due to photodisintegration. This strong inverse reaction flow could limit mass transfer through the *rp*-process, with the proton capture rate on ^{23}Al critically determining the amount of reaction flow through this path in the network.

The sensitivity to the ^{22}Mg(α,p) reaction rate (see Figure 5.9) could be related to the limited flow through ^{23}Al, since this reaction rate determines the relative flow through a branching just below ^{23}Al(p,γ). Increasing the ^{22}Mg(α,p) rate would lead this (α,p) branch to bypass ^{23}Al at a reduced temperature and therefore at earlier times during burst rise. So it is surprising that the upper limit rate for ^{22}Mg(α,p) results in a *reduced* luminosity after the burst peak. This may be the result of compositional inertia. The extended tail generated by the upper limit rate may be explained by an increased proton-to-seed ratio resulting from the earlier use of a bridging (α,p) reaction.

The ^{59}Cu(p,γ) rate (see Figure 5.6) likely affects the proportion of reaction flow through a previously identified reaction cycle [19], similar in operation to the CNO cycle, with this proton capture competing with the (p,α) reaction that closes the cycle. Reaction cycling is also a possible explanation for the sensitivity to the ^{61}Ga(p,γ) reaction rate, which may also be in competition with a significant (p,α) branch.

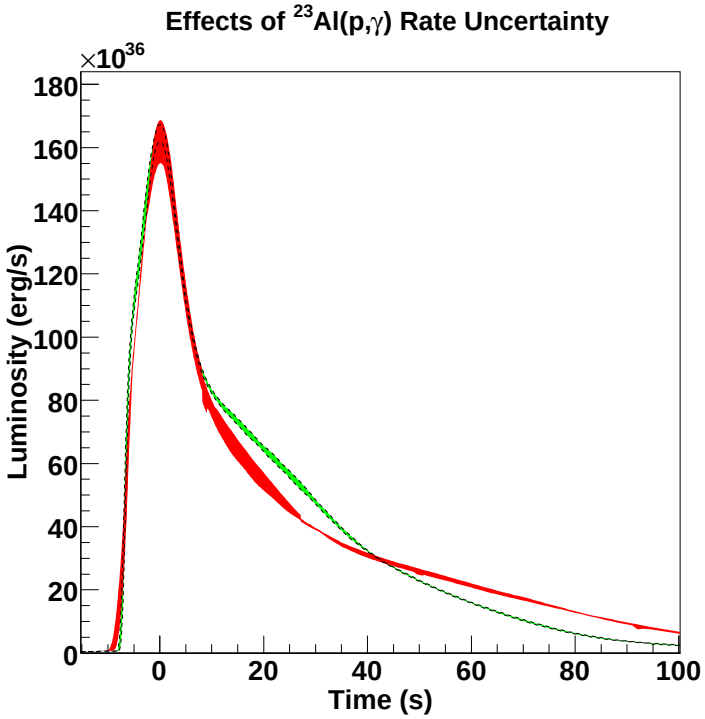

Figure 5.4: Multi-zone burst lightcurve 1σ confidence intervals are shown for an upper limit [green] and lower limit [red] ^{23}Al(p,γ) rate.

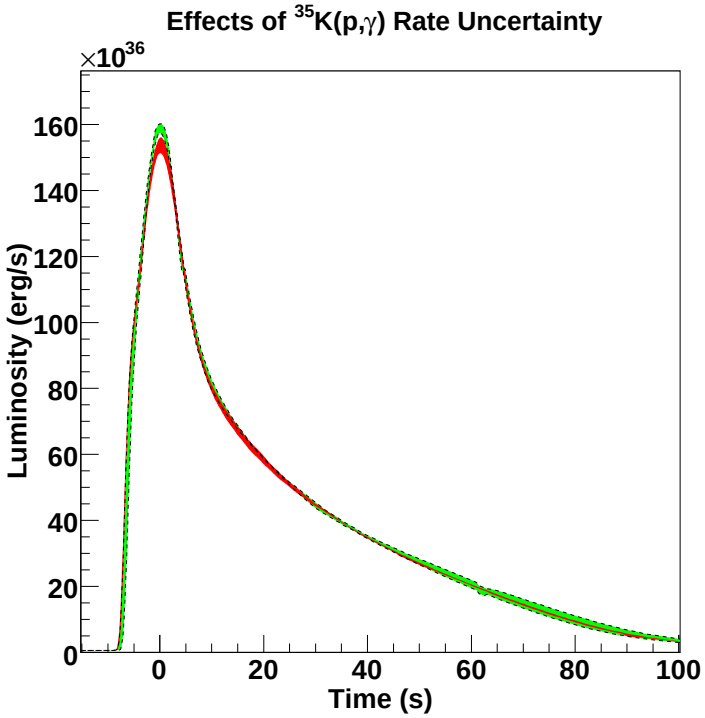

Figure 5.5: Multi-zone burst lightcurve 1σ confidence intervals are shown for an upper limit [green] and lower limit [red] ^{35}K(p,γ) rate.

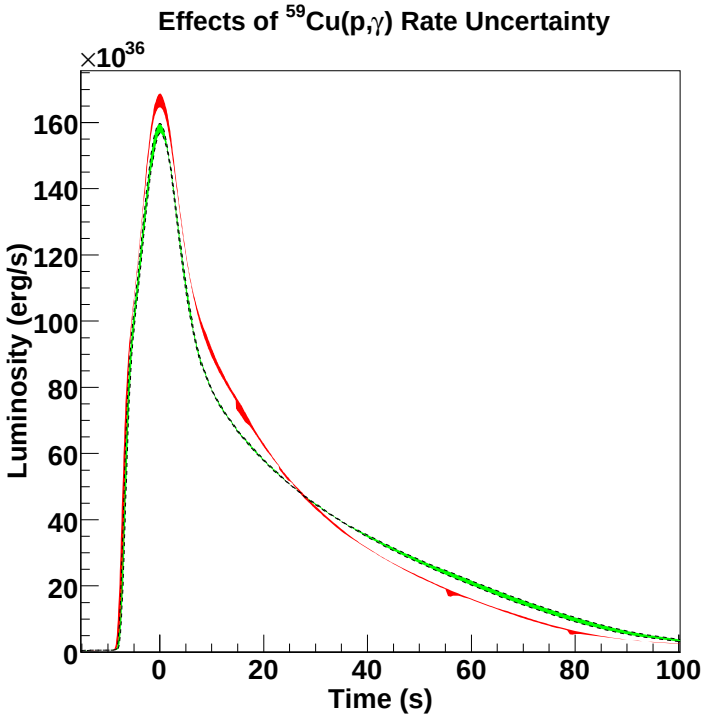

Figure 5.6: Multi-zone burst lightcurve 1σ confidence intervals are shown for an upper limit [green] and lower limit [red] ^{59}Cu(p,γ) rate.

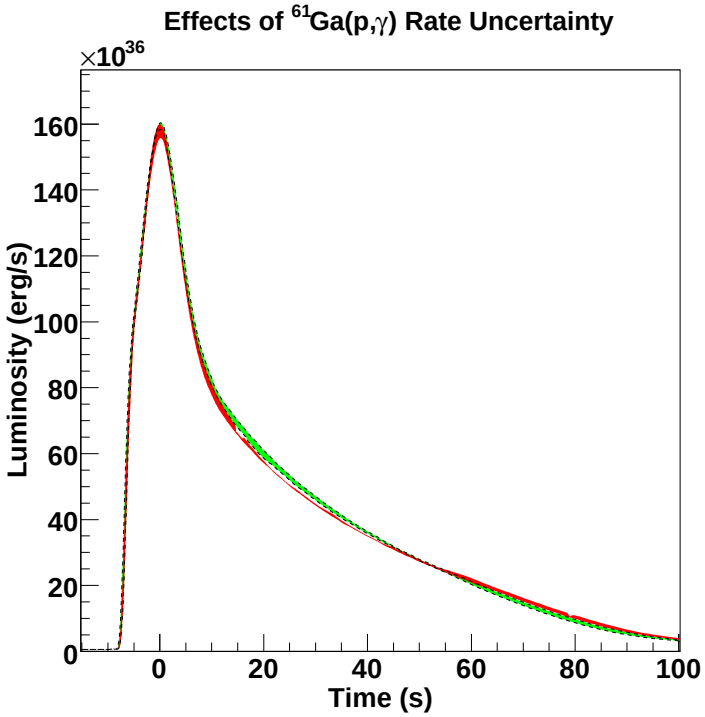

Figure 5.7: Multi-zone burst lightcurve 1σ confidence intervals are shown for an upper limit [green] and lower limit [red] ^{61}Ga(p,γ) rate.

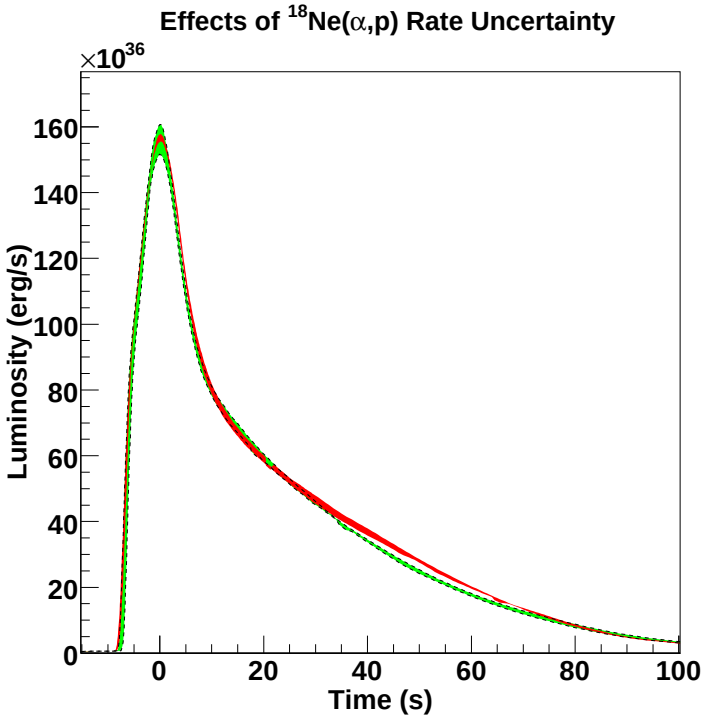

Figure 5.8: Multi-zone burst lightcurve 1σ confidence intervals are shown for an upper limit [green] and lower limit [red] ^{18}Ne(α,p) rate.

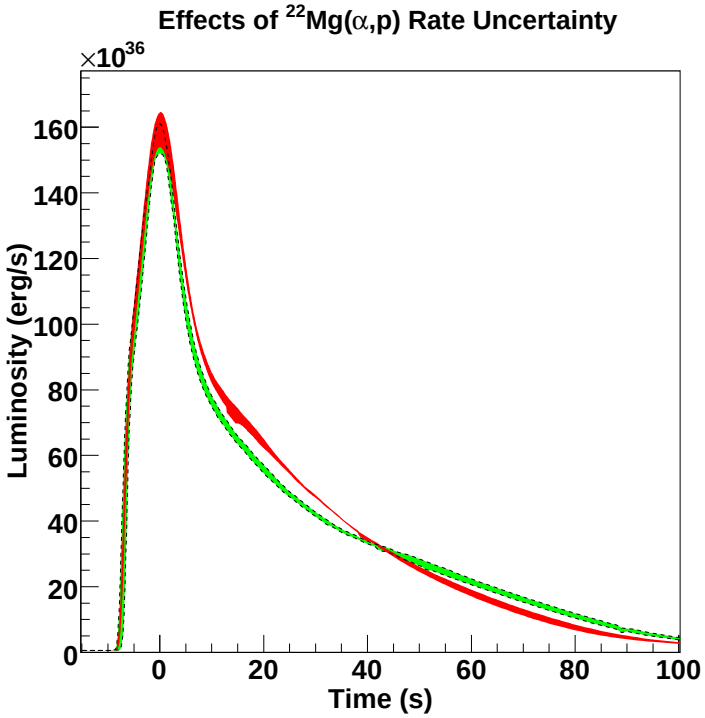

Figure 5.9: Multi-zone burst lightcurve 1σ confidence intervals are shown for an upper limit [green] and lower limit [red] ^{22}Mg(α,p) rate.

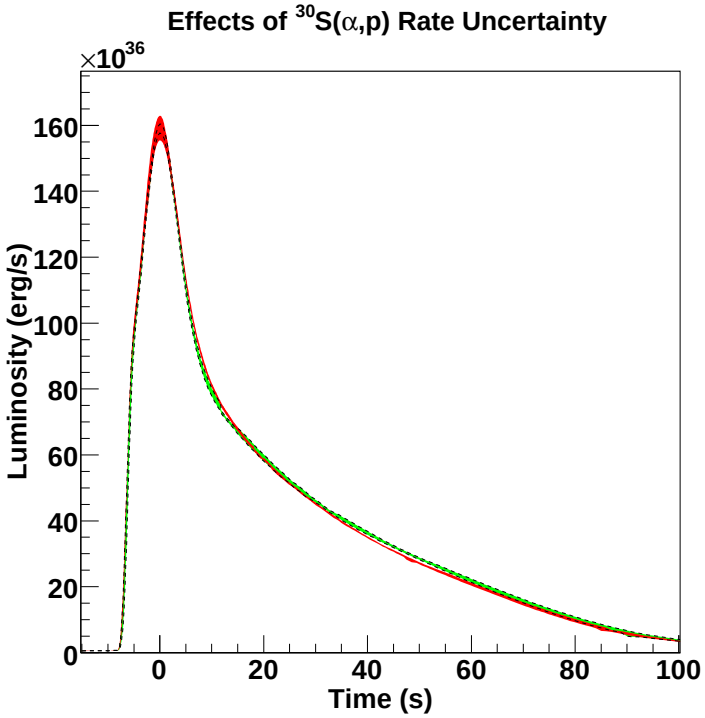

Figure 5.10: Multi-zone burst lightcurve 1σ confidence intervals are shown for an upper limit [green] and lower limit [red] ^{30}S(α,p) rate.

Chapter 6

Conclusions and Outlook

6.1 Summary

We have completed an experimental study to measure excited states in two isotopes along the *rp*-process path, ^{37}Ca and ^{36}K. The measured excited state energies for levels above the proton threshold were the dominant uncertainty in the resonant capture dominated reaction rates ^{36}K(p,γ) and ^{35}Ar(p,γ). The former was shown to be an important reaction and possible waiting point in previous X-ray burst model studies, largely because of its position relative to ^{36}K, which is vulnerable to photodisintegration at burst temperatures because of its fairly low proton separation energy. Simulations in the Kepler X-ray burst code show that the burst lightcurve is not sensitive to this reaction rate in a steady-state bursting scenario in the specific accretion model used, while the model does show sensitivity to the ^{36}K(p,γ) reaction rate for bursts at the onset of bursting behavior.

A study of the sensitivity of Type I X-ray burst's lightcurves to a comprehensive set of (p,γ) and (α,p) reaction rates for a specific accretion model has been completed. The study used a specifically calibrated single-zone burst code for a broad search with a liberal assumption of reaction rate uncertainties followed by individual simulations in a multi-zone code for reaction rates identified as important in the single-zone study.

Uncertainties for the multi-zone simulations were specifically estimated based on the current state of knowledge of the particular reaction rate. Several important reaction rates have been identified for which experimental effort is needed to reduce the rate uncertainty and constrain the model lightcurve.

6.2 Conclusions

The dramatically different ^{36}K(p,γ)^{37}Ca reaction rate, roughly a factor of 10^4 higher than the previously estimated value, results in significant changes to the first burst lightcurve in the MZ model of the KEPLER code. The fact that the increased rate does not significantly change the median lightcurve in this model simulated in a steady state bursting scenarioserves to emphasize both the effects of compositional inertia in the burst lightcurve and the importance of sensitivity studies, since it clearly cannot be assumed that experimental effort is justified merely by the magnitude of uncertainty in a particular reaction rate along the *rp*-process path. Further analysis will reveal if the rate has any affect on the ashes produced, though generally large changes in the ashes are strongly correlated with changed lightcurves.

The relatively small set of critical rate uncertainties identified in the sensitivity study gives some hope that the goal of eliminating the dominant nuclear physics uncertainties in the X-ray burst *rp*-process is within reach. Although similar consideration of other bursting scenarios and other nuclear physics inputs is necessary to determine the full set of critical nuclear physics uncertainties.

Whether the rp-process is a significant means of galactic nucleosynthesis is a question still unanswered. The p-process of photodisintegration, together with the rapid and slow neutron capture processes, may be sufficient to account for the "p-process" nuclear abundances observed, and it is at least widely thought to be unlikely that large amounts of material are ever able to escape the gravitational well of the neutron star, though some suggest photospheric radius expansion bursts may eject some ma-

terial. The ashes of rp-process burning are more likely slowly incorporated into the neutron star crust. However, as noted by Schatz et al. in [15], overproduction of certain p-nuclei by the rp-process together with predicted insufficient production of these same isotopes in the p-process suggest the possibility that material from rp-process nucleosynthesis in Type I X-ray bursts is somehow contributing to galactic isotopic abundances. Naturally, if this is possible, the contribution from rp-nucleosynthesis would not be limited only to these isotopes; the contribution from overproduction of other species would also have to be studied, some of which may lead to further inconsistencies. Even if there is no contribution from rp-process nucleosynthesis to the observed abundance distribution, this does little to detract from the value of exploring such systems. In either case they serve as a means of testing our understanding of nuclear structure as well as nuclear and thermodynamic processes at extreme temperatures and densities.

6.3 Outlook

Reducing the (p,γ) and (α,p) reaction rate uncertainties identified in Chapter 5 as the dominant reaction rate based uncertainties in the ZM model of Kepler should be made a top priority of experimental work. New facilities recently completed in Japan and proposed in the US and Europe will greatly improve access to the proton-rich isotopes to be studied, and advanced γ-ray tracking arrays will improve the resolution of in-flight methods, such as that used in the experiment discussed in this work. Such methods are often required given the short lifetime of the isotopes to be studied.

In this same direction, a more complete effort is needed to calibrate our best burst models to the full range of burst behavior, including a range of accreted abundances, accretion rates, surface gravities, etc. Sensitivity studies should be extended to include at least some representative cross section of the full range of observed bursts. Only a single physical model was considered here. Other physical model parameters

would be expected to result in a different reaction flow and show new sensitivities to nuclear reaction rates.

The calibrated single-zone code has proved successful at identifying reaction rate sensitivities present in the multi-zone KEPLER model. The two step method could be expanded to include higher-order sensitivities, that is a sensitivity to a simultaneous variation of multiple rates within their uncertainties that is not present in an individual rate study. Other nuclear physics quantities must be considered in the same way: atomic masses, beta decay rates, S-factors, spectroscopic factors, etc. If resources become available, an expanded sensitivity study in the multi-zone code may reveal other important nuclear data needs not identified in the single-zone study.

The sensitivity study should not be viewed as the end, since it is only the first step. Once the burst models are better constrained there is much progress to be made in our understanding of the process itself. How does compositional inertia influence the burst ignition, energy generation, and nucleosynthesis? What is the composition of the final ashes that are incorporated into the NS crust after repeated burning due to thermal pulses from superstitial bursts? So in the study of Type I X-ray bursts there is both much promise of substantial progress in the near future and much work yet to be done.

Bibliography

[1] H. Schatz, A. Aprahamian, V. Barnard, L. Bildsten, A. Cumming, M. Ouellette, T. Rauscher, F.-K. Thielemann, and M. Wiescher. End point of the *rp* process on accreting neutron stars. *Phys. Rev. Lett.*, 86(16):3471–3474, Apr 2001.

[2] B. Fields and S. Sarkar. Big-bang nucleosynthesis (particle data group mini-review). *astro-ph/0601514v2*, 2006.

[3] Richard Boyd. *Introduction to Nuclear Astrophysics*. University of Chicago Press, 2008.

[4] D. K. Galloway, A. Cumming, E. Kuulkers, L. Bildsten, D. Chakrabarty, and R. E. Rothschild. Periodic thermonuclear x-ray bursts from GS 1826–24 and the fuel composition as a function of accretion rate. *Astrophysical Journal*, 601:466, 2004.

[5] Edward F. Brown and Lars Bildsten. The ocean and crust of a rapidly accreting neutron star: Implications for magnetic field evolution and thermonuclear flashes. *The Astrophysical Journal*, 496(2):915–933, 1998.

[6] S. S. Gupta et al. Neutron reactions in accreting neutron stars: a new pathway to efficient crust heating. *arXiv:0811.1791v1[astro-ph]*, Nov 2008.

[7] Walter H. G. Lewin, Jan van Paradijs, and Ronald E. Taam. X-ray bursts. *Space Science Reviews*, 62:223–389, 1993.

[8] T. E. Strohmayer and L. Bildsten. *Compact Stellar X-ray Sources*, chapter New Views of Thermonuclear Bursts. Cambridge: Cambridge University Press, 2006.

[9] H. Schatz and K. E. Rehm. X-ray binaries. *Nucl. Phys. A*, 777:601–622.

[10] C. J. Hansen and H. M. van Horn. Steady-state nuclear fusion in accreting neutron-star envelopes. *Astrophysical Journal*, 195:735–741, February 1975.

[11] R. K. Wallace and S. E. Woosley. Explosive hydrogen burning. *Astrophysical Journal Supplement Series*, 45:389, 1981.

[12] L. Bildsten. Theory and observations of type I x-ray bursts from neutron stars. In S. S. Holt and W. W. Zhang, editors, *Cosmic Explosions - proceeding of the 10th Annual October Astrophysics Conference*, 2000.

[13] D. Galloway, 2008. Private communication.

[14] Randall L. Cooper and Ramesh Narayan. Theoretical models of superbursts on accreting neutron stars. *The Astrophysical Journal*, 629(1):422–437, 2005.

[15] H. Schatz and M. Wiescher T. Rauscher J. F. Rembges F.-K. Thielemann B. Pfeiffer P. Möller K.-L. Kratz H. Herndl B. A. Brown H. Rebel A. Aprahamian, J. Görres. rp-process nucleosynthesis at extreme temperature and density conditions. *Phys. Rep.*, 294:167–263, 1998.

[16] S. E. Woosley, A. Heger, A. Cumming, R. D. Hoffman, J. Pruet, T. Rauscher, J. L. Fisker, H. Schatz, B. A. Brown, and M. Wiescher. Models for type I x-ray bursts with improved nuclear physics. *Astrophysical Journal Supplement Series*, 151:75–102, 2004.

[17] Alexander Heger, Andrew Cumming, Duncan K. Galloway, and Stanford E. Woosley. Models of type i x-ray bursts from gs 1826–24: A probe of rp-process hydrogen burning. *The Astrophysical Journal Letters*, 671(2):L141–L144, 2007.

[18] A. Cumming. Thermonuclear x-ray bursts: Theory vs. observations. *astro-ph/0309626v2*, May 2003.

[19] L. van Wormer, J. Görres, C. Iliadis, and M. Wiescher. Reaction rates and reaction sequences in the rp-process. *Astrophysical Journal*, 432:326–350, 1994.

[20] S. Bishop et al. ^{21}Na(p,γ)^{22}Mg reaction and oxygen-neon novae. *Phys. Rev. Lett.*, 90:162501, 2003.

[21] J. L. Fisker, V. Barnard, J. Görres, K. Langanke, M. Martínez-Pinedo, and M. C. Wiescher. Shell model based reaction rates for rp-process nuclei in the mass range a = 44–63. *At. Data and Nucl. Data Tables*, 79:241–292, 2001.

[22] T. Rauscher, F.-K. Thielemann, and K. L. Kratz. Nuclear level density and the determination of thermonuclear rates for astrophysics. *Phys. Rev. C*, 56:1613, 1997.

[23] R. R. C. Clement, D. Bazin, W. Benenson, B. A. Brown, A. L. Cole, M. W. Cooper, P. A. DeYoung, A. Estrade, M. A. Famiano, N. H. Frank, A. Gade, T. Glasmacher, P. T. Hosmer, W. G. Lynch, F. Montes, W. F. Mueller, G. F. Peaslee, P. Santi, H. Schatz, B. M. Sherrill, M-J. van Goethem, and M. S. Wallace. New approach for measuring properties of *rp*-process nuclei. *Phys. Rev. Lett.*, 92(17):172502, Apr 2004.

[24] H. T. Fortune, R. Sherr, and B. A. Brown. Coulomb energies in ^{17}Ne and the ground state mass of ^{18}Na. *Phys. Rev. C*, 73(6):064310, 2006.

[25] Walter Benenson and Edwin Kashy. Isobaric quartets in nuclei. *Rev. Mod. Phys.*, 51(3):527–540, 1979.

[26] Bernard E. J. Pagel. *Nucleosynthesis and Chemical Evolution of Galaxies*. Cambridge University Press, Cambridge, UK, 1997.

[27] R. R. C. Clement. *A New Method for Nuclear Structure Measurement of Neutron Deficient Nuclei*. PhD thesis, Michigan State University, 2003.

[28] D. J. Morrissey and B. M. Sherrill. *The Euroschool Lectures on Physics with Exotic Beams*, volume 1, chapter In-Flight Separation of Projectile Fragments. Springer Berlin / Heidelberg, 2004.

[29] D. J. Morrissey, B. M. Sherrill, M. Steiner, A. Stolz, and I. Wiedenhoever. Commissioning the A1900 projectile fragment separator. *Nucl. Instr. and Meth. B*, 204:90–96, 2003.

[30] D. Bazin, J. A. Caggiano, B. M. Sherrill, J. Yurkon, and A. Zeller. The S800 spectrograph. *Nucl. Instr. and Meth. B*, 204:629–633, 2003.

[31] W. F. Mueller, J. A. Church, T. Glasmacher, D. Gutknecht, G. Hackman, P. G. Hansen, Z. Hu, K. L. Miller, and P. Quirin. Thirty-two-fold segmented germanium detectors to identify γ-rays from intermediate-energy exotic beams. *Nucl. Instr. and Meth. A*, 466:492–498, 2001.

[32] M. Berz, K. Joh, J. A. Nolen, B. M. Sherrill, and A. F. Zeller. Reconstructive correction of aberrations in nuclear particle spectrographs. *Phys. Rev. C*, 47(2):537–544, 1993.

[33] D.-C. Dinca. *Study of the Development of Shell Closures at N=32,34 and Approaches to Sub-Segment Interaction-Point Determination in 32-Fold Segmented High-Purity Germanium Detectors*. PhD thesis, Michigan State University, 2005.

[34] Rene Brun and Fons Rademakers. Root - an object oriented data analysis framework. In *Proceedings AIHENP'96 Workshop, Lausanne*, volume 389, pages 81–86. Nucl. Instr. and Meth. A, 1996.

[35] D. Galaviz, 2006. Private communication.

[36] M. Matoš, 2007. Private communication.

[37] D. Weisshaar, 2005. Private communication.

[38] P. M. Endt and R. B. Firestone. Supplement to energy levels of A = 2144 nuclei (VII). *Nucl. Phys. A*, 633:1, 1998.

[39] W. Benenson, E. Kashy, and I. D. Proctor. Isobaric mass quartets in the mass-21 and mass-37 nuclei. *Phys. Rev. C*, 8(1):210–215, Jul 1973.

[40] B. A. Brown, 2005. Private communication.

[41] H. Herndl, J. Görres, M. Wiescher, B. A. Brown, and L. Van Wormer. Proton capture reaction rates in the *rp* process. *Phys. Rev. C*, 52:1078, 1995.

[42] T. G. Dzubay, A. A. Jaffe, E. J. Ludwig, T. A. White, F. Everling, D. W. Miller, and D. A. Outlaw. Energy levels of ^{36}K. *Physics Letters B*, 33(4):302–304, Oct 1970.

[43] W. Trinder, E. G. Adelberger, B. A. Brown, Z. Janas, H. Keller, K. Krumbholz, V. Kunze, P. Magnus, F. Meissner, A. Piechaczek, M. Pfützner, E. Roeckl, K. Rykaczewski, W. D. Schmidt-Ott, and M. Weber. Study of the β decays of ^{37}Ca and ^{36}Ca. *Nuclear Physics A*, 620(2):191–213, Jul 1997.

[44] C. Iliadis, 2008. Private communication.

[45] P. Doornenbal, P. Reiter, H. Grawe, T. Otsuka, A. Al-Khatib, A. Banu, T. Beck, F. Becker, P. Bednarczyk, G. Benzoni, A. Bracco, A. Bürger, L. Caceres, F. Camera, S. Chmel, F. C. L. Crespi, H. Geissel, J. Gerl, M. Górska, J. Grębosz, H. Hübel, M. Kavatsyuk, O. Kavatsyuk, M. Kmiecik, I. Kojouharov, N. Kurz, R. Lozeva, A. Maj, S. Mandal, W. Meczynski, B. Million, Zs. Podolyák, A. Richard, N. Saito, T. Saito, H. Schaffner, M. Seidlitz, T. Striepling, Y. Utsuno, J. Walker, N. Warr, H. Weick, O. Wieland, M. Winkler, and H. J. Wollersheim. The T=2 mirrors ^{36}Ca and ^{36}S: A test for isospin symmetry of shell gaps at the driplines. *Physics Letters B*, 647(4):237–242, Apr 2007.

[46] A. Bürger, F. Azaiez, M. Stanoiu, Zs. Dombrádi, A. Algora, A. Al-Khatib, B. Bastin, G. Benzoni, R. Borcea, Ch. Bourgeois, P. Bringel, E. Clément, J.-C. Dalouzy, Z. Dlouhý, A. Drouart, C. Engelhardt, S. Franchoo, Zs. Fülöp, A. Görgen, S. Grévy, H. Hübel, F. Ibrahim, W. Korten, J. Mrázek, A. Navin, F. Rotaru, P. Roussel-Chomaz, M.-G. Saint-Laurent, G. Sletten, D. Sohler, O. Sorlin, Ch. Theisen, C. Timis, D. Verney, and S. Williams. Spectroscopy around ^{36}Ca. *Acta Physica Polonica B*, 38:1353, 2007.

[47] F. Della Vedova et al. Isospin symmetry breaking at high spin in the mirror nuclei ^{35}Ar and ^{35}Cl. *Phys. Rev. C*, 75, 2007.

[48] R. Ringle, T. Sun, G. Bollen, D. Davies, M. Facina, J. Huikari, E. Kwan, D. J. Morrissey, A. Prinke, J. Savory, P. Schury, S. Schwarz, and C. S. Sumithrarachchi. High-precision penning trap mass measurements of ^{37,38}Ca and their contributions to conserved vector current and isobaric mass multiplet equation. *Phys. Rev. C*, 75(5):055503, 2007.

[49] A. Garca, E. G. Adelberger, P. V. Magnus, H. E. Swanson, O. Tengblad, ISOLDE Collaboration, and D. M. Molz. β^+ decays of ^{37}Ca: Implications for the efficiency of the ^{37}Cl solar ν detector. *Phys. Rev. Lett.*, 67(26):3654–3657, Dec 1991.

[50] A. Matthew Amthor, Daniel Galaviz, Alexander Heger, Alexander Sakharuk, Hendrik Schatz, and Karl Smith. Sensitivity of type I x-ray bursts to rp-process reaction rates. In *proceedings of International Symposium on Nuclear Astrophysics - Nuclei in the Cosmos - IX*, 2006. PoS(NIC-IX)068.

[51] Anuj Parikh, Jordi Jose, Fermin Moreno, and Christian Iliadis. The effects of variations in nuclear processes on type I x-ray burst nucleosynthesis. Submitted to The Astrophysical Journal Supplement Series.

[52] Richard Cyburt et al. Reaclib v1.0. Unpublished.

[53] G. R. Caughlan and W. A. Fowler. Thermonuclear reaction rates v. *At. Data and Nucl. Data Tables*, 40:283–334, 1988.

[54] H. O. U. Fynbo et al. Revised rates for the stellar triple-α process from measurement of ^{12}c nuclear resonances.

[55] A. Sakharuk et al. An updated library of reaction rates for the astrophysical *rp*-process. In *12th International Symposium on Capture Gamma-Ray Spectroscopy and Related Topics*, number 819 in AIP Conf. Proc., pages 118–122, 2006.

[56] G. Audi, A. H.Wapstra, and C. Thibault. The ame 2003 atomic mass evaluation ii. *Nucl. Phys. A*, 729:337–676, 2003.

[57] T. Rauscher and F.-K. Thielemann. Astrophysical reaction rates from statistical model calculations. *At. Data and Nucl. Data Tables*, 75:1–351, 2000.

[58] J. K. Tuli. Nuclear wallet cards. *National Nuclear Data Center*, 2007.